

Glowing to flaming transition in Douglas fir with varied moisture content

Jorge Valdivia, Xiuqi Xi^{**}, Albert Simeoni, James L. Urban*

Department of Fire Protection Engineering, Worcester Polytechnic Institute, 100 Institute Road, Worcester, MA 01609, USA

Abstract

In wildfires, vegetation can ignite through convective and radiative heating, influenced by factors like wind and fire size. Understanding ignition from these modes is crucial for computational fire models. This study investigates the ignition behavior of Douglas fir branches under convective heating using a custom apparatus, thermogravimetric analysis (TGA), and computational simulations in Fire Dynamics Simulator (FDS). Ignition delay times were determined from color camera recordings. In all experiments resulting in flaming ignition, glowing combustion preceded it. Fuel moisture content (FMC) significantly impacted ignition, with higher FMC delaying ignition and reducing ignition probability, while lower FMC increased the likelihood of ignition. In tests with flaming ignition, gas-phase ignition occurred near the fuel sample in most cases, though in some, it occurred farther away. High-speed imaging was used to track ignition location and flame propagation when gas-phase ignition occurred at a distance from the sample. TGA revealed how thermal decomposition influenced ignition dynamics. Computational modeling aligned with experimental findings and clarified the role of heat transfer, fuel properties, and FMC on combustion. These results enhance the understanding of vegetation ignition and fire dynamics under convective heating conditions.

Keywords: Convective heating, Convective ignition, Glowing combustion, TGA, FMC, Douglas fir

1. Introduction

Wildfires in recent years have demonstrated the vulnerability of the urban environment to wildfire. In wildland-urban interface (WUI) fires, structure ignition can occur through direct flame contact (convection and radiation), flame radiation, or firebrand spotting [1, 2]. Beginning in the mid-1990s, defensible space has been promoted as a reliable strategy to mitigate wildfire risk [3, 4]. This refers to an area around a building where vegetation, debris, and other combustible fuels are treated, cleared, or reduced to slow fire spread, limit heating, and reduce firebrand spotting. Although defensible space has proven effective, it often relies on empirical clearance distance rules, and its underlying mechanisms remain not fully understood.

To understand the ignition process and the mechanisms driving discontinuous fire spread in the WUI, it is essential to analyze the fundamental bench-scale phenomena in controlled laboratory settings. In these scenarios, both radiative and convective heat transfer significantly influence the ignition of vegetation [1, 2]. One of the primary factors affecting these ignition processes is the fuel moisture content (FMC), defined as the mass of water contained within vegetation relative to its dry mass. FMC is a key variable in many fire behavior prediction models and fire danger indices, as it influences several critical aspects of fire dynamics, including ignition susceptibility, combustion, fuel availability, fire severity, and spread, as well as smoke generation and composition [5–8].

Radiation is an important mechanism for heat transfer mechanism in wildfires. Williams [2] identified two main sub-categories for studying radiation: radiation from flames and radiation from burning fuel surfaces. Experiments using apparatuses such as the Cone Calorimeter [9–12] and the Fire Propagation Apparatus [13–15] have been extensively conducted to characterize the ignition and fire phenomena of vegetation samples under incident radiative heat fluxes. In specific conditions, theoretical models for ignition delay times of solid fuels, such as the one developed by Spearpoint and Quintiere [16], have been applied when radiation is the primary heat transfer mechanism, among others that raised from applying an energy balance in either the porous media or the fuel element, e.g., Refs. [17, 18]. Convective heat transfer is also important, with the strongest scenario often occurring when the fuel is in direct contact with the flames [19–22], i.e., flame impingement. Furthermore, during a wildfire, upward convection currents occur, where hot gases released from the flames and the fire plume transport heat, smoke, and embers vertically. When wind is significant, horizontal spread becomes prominent: the wind can carry the heated air horizontally, and this forced convection can drive the fire front forward, spreading the flames over a larger area.

Convective heating in solid fuels ignition and propagation has also been investigated. Fernandez-Pello [23] discussed the theoretical aspects of convective heating of solids (PMMA, PVC, among others) and the governing equations for the solid-phase ignition, based on the experiments and findings of Niioka [24]. More recently, Roenner and Rein [25] developed an apparatus to investigate the ignition of polymers from convective heating, finding ignition temperatures 10% lower than previously

*Corresponding author. Email: jurban@wpi.edu

**Corresponding author. Email: xxi1@wpi.edu

Nomenclature

Latin letters

\dot{q}''	Heat flux ($\text{kW}\cdot\text{m}^{-2}$)
A	Pre-exponential factor (s^{-1})
b	Intercept of the linear fit (-)
C	Calibration coefficient of the pitot probe (-)
c_p	Specific heat capacity ($\text{J}\cdot\text{kg}^{-1}\cdot\text{K}^{-1}$)
D	Diameter (m)
d	Internal diameter of the plenum (mm)
dA	Differential disk element (m^2)
E_a	Activation energy ($\text{kJ}\cdot\text{mol}^{-1}$)
$F_{i \rightarrow j}$	View factor from surface i to surface j (-)
H	Height of the conditioning section (mm)
h	Heat transfer coefficient ($\text{W}\cdot\text{m}^{-2}\cdot\text{K}^{-1}$)
k	Thermal conductivity ($\text{W}\cdot\text{m}^{-1}\cdot\text{K}^{-1}$)
L	Height (cm)
l	Height of the flow straightener (mm)
m	Mass (g)
p	Pressure (Pa)
R	Gas constant ($\text{J}\cdot\text{mol}^{-1}\cdot\text{K}^{-1}$)
T	Temperature ($^\circ\text{C}$)
t	Time (s)
v	Velocity ($\text{m}\cdot\text{s}^{-1}$)
W	Weight (g)
z	Sample location above the plenum (mm)
Nu	Nusselt number (-)

Greek letters

α	Conversion degree (-)
β	Heating rate ($\text{K}\cdot\text{min}^{-1}$)
Δ	Difference (-)
ℓ_{ig}	Ignition location (cm)
γ	Regression coefficients

ρ	Density ($\text{kg}\cdot\text{m}^{-3}$)
σ	Stefan-Boltzmann constant ($\text{W}\cdot\text{m}^{-2}\cdot\text{K}^{-4}$)
ε	Emissivity (-)
ζ	Mixed fraction (-)

Subscripts

∞	Ambient
$conv$	Convection
cr	Critical
cyl	Cylinder
d	Dry
f	Flame
fr	Fresh
fs	Flow straightener
gas	Gas
$glow$	Glowing
ig	Ignition
inc	Incident
k	Pine needle
m	Metallic surfaces
$prop$	Propagation
rad	Radiation
$re - rad$	Radiative losses
s	Solid
mix	Mixing

Acronyms

FMC	Fuel moisture content (%)
HRR	Heat release rate (kW)
HRRPUV	Heat release rate per unit volume ($\text{kW}\cdot\text{m}^{-3}$)
MLR	Mass loss rate ($\text{kg}\cdot\text{s}^{-1}$)

reported in the literature. For wildland fuels, McAllister and Finney [26] examined the ignition delay times of dowel rods subjected to primarily convective heating, using both thermally 60 thin and thick heat transfer approaches to theoretically determine ignition delay times. They observed gas-phase autoignition of the dowels for gas temperatures over $600\text{ }^\circ\text{C}$. Additionally, McAllister et al. [27] investigated the convective ignition of various wildland fuels with different moisture contents, including pine, fir, and chaparral, under a constant gas temperature. They found that at $500\text{ }^\circ\text{C}$, all dead fuels exhibited flaming ignition, whereas live fuels primarily showed glowing ignition. Phillips and Becker [28] examined the burning behavior of white pine sticks in a high-temperature wind tunnel. They 70 observed that when the gas temperature exceeded $410\text{ }^\circ\text{C}$, glowing combustion occurred on the surface of the sticks, leading to

circumferential and longitudinal cracking of the char layer. At temperatures of $800\text{ }^\circ\text{C}$ and above, flaming ignition of pyrolysis gases was reported to occur within seconds.

75 Glowing (smoldering) combustion has been observed in experiments involving wood samples subjected to radiative heating with piloted ignition. For example, Schroeder [29] reported glowing combustion at low heat fluxes ($\dot{q}_{inc}'' \leq 20\text{ kW}\cdot\text{m}^{-2}$) in four species of wood slabs (Red Oak, Maple, Douglas fir, and Redwood), which subsequently led to (localized) flaming ignition. Spearpoint and Quintiere [16] discussed these findings in their integral ignition model, highlighting the need for further research to better understand the role of glowing combustion in the piloted ignition of wood. A year later, Boonmee and Quintiere [30] studied both glowing and flaming au-

to ignition of wood in the cone calorimeter, defining and examining two modes of autoignition: glowing and flaming, and comparing them to piloted ignition. They found that flaming autoignition occurs at high incident heat fluxes, where pyrolysis products mix with air to form a combustible mixture, while glowing autoignition occurs at low incident heat fluxes, where surface oxidation leads to glowing spots on the sample surface. Later, the same authors [31] conducted a theoretical analysis on surface glowing ignition leading to flaming ignition by numerically solving both the solid and gas phases. Their results categorized flaming autoignition based on incident heat flux: for $\dot{q}_{inc}'' \geq 40 \text{ kW}\cdot\text{m}^{-2}$, gas-phase flaming autoignition occurs shortly after solid-phase glowing ignition, while at fluxes below $40 \text{ kW}\cdot\text{m}^{-2}$, a considerable delay follows solid-phase glowing ignition before flaming autoignition occurs.

Simulations have also been conducted to gain a deeper understanding of the ignition processes [32], where an infinitely fast chemistry model was employed to simulate ignition. The simulated mass loss was compared with experimental results, showing that the simulation can effectively represent the experimental observations.

Despite research investigating the ignition of wildland fuels by hot gas flows (convection) [26–28], the topic is less studied than radiation heating and there still remains no research investigating the critical conditions for ignition by convective heating. Moreover, the ignition processes in numerical simulations are not fully represented because of the use of the infinitely fast chemistry model that assumes that combustion occurs instantaneously whenever fuel comes into contact with oxygen, bypassing the complex intermediate reactions and ignition delays that are characteristic of real-world combustion processes. Additionally, mesh resolution plays a critical role in computational fire modeling, especially in determining the accuracy of heat transfer, flame structure, and ignition dynamics [32, 33]. In the context of wildland fires, however, high-resolution simulations are often computationally prohibitive due to the vast spatial domains and long simulation durations required. As a result, modeling approaches that maintain reasonable physical fidelity under coarser mesh conditions are essential for practical and operational use [34]. This study addresses this gap by examining the physical processes governing the critical ignition conditions of Douglas fir foliage with varying fuel moisture contents (FMC) in hot convective flows at different temperatures as well as the ignition behavior from convective heating. Moreover, this study also investigates whether a phenomenological ignition approach, specifically the spark model combined with infinitely fast chemistry, can effectively reproduce ignition behavior under coarse mesh conditions representative of wildland fire simulations. The research integrates bench-scale experiments, computational modeling, and milligram-scale material characterization (e.g., thermogravimetric analysis) to better represent the autoignition process. The findings aim to enhance the development of physics-based fire modeling frameworks, improving wildfire exposure assessments at the WUI and informing the design of effective defensible spaces through computational fire modeling.

2. Methods

2.1. Convective ignition facility

Douglas fir sprigs (small branch and foliage/needles) at different fuel moisture contents were ignited by rapid introduction to a flow of hot air. The experiments were performed in a bench-scale apparatus called Convective Ignition Facility (CIF), which is shown in Fig. 1a and is loosely based on similar devices used by other researchers [26, 27]. The CIF is composed of a pneumatic gas supply system, a 10 kW “Airtorch” process heater (MHI Inc.), a flow conditioning section, and an experimental area above the outlet of the flow conditioning section. The pneumatic system filters (PR/Filter) compressed house air and regulates it to a pressure of 20 psi which is metered with a mass flow controller (MFC – Aalborg DPC77). The Mass flow controller is capable of managing airflow up to 1,000 L·min⁻¹ and can be controlled by a computer. For safety, a pressure relief valve (PRV) is installed between the mass flow controller and the Airtorch. The controlled airflow enters the Airtorch, where it is heated by resistance heaters regulated by an external power supply equipped with a Proportional-integrated-derivative (PID) controller. The heated flow enters the flow conditioning plenum (cf. Fig. 1b) constructed with ceramic boards and a central metal tube-insert with an internal diameter of $d = 5.75''$ (146 mm). Between the metal tube and the ceramic boards, a thin layer of ceramic fiber insulation was placed. Within the flow conditioning section, the air enters a plenum and then passes through two steel perforated sheets and a flow straightener built out of welded low carbon-steel tubes with a length of $l = 3''$ (76.2 mm) and an internal diameter of 0.47'' (11.94 mm). Above the outlet of the flow conditioning section, the sample holder allows for the insertion and positioning of the sample at a height of $z = 3.5''$ (88.9 mm) above the top of the conditioning section, as illustrated in Fig. 1b.

2.2. Gas temperature and velocity measurements

Gas temperature and velocity measurements are taken before experiments to verify steady-state flow and quantify experimental conditions (temperature and flow velocity). For temperature measurements, a fine (36 AWG – 0.127 mm) bare junction Type-K thermocouple with fiberglass insulation (Omega 5TC-GG-K-30-36) was positioned at the same height as the fuel sample, z , (cf. Fig. 1b) above the top of the conditioning section, along the centerline of the hot gas outlet. Thermocouple correction was applied following the method outlined by Ren et al. [35], ensuring accuracy in the gas temperature measurements. However, due to the thermocouple’s fine diameter, the effects of incident radiation and re-radiation were negligible (less than 2 °C for all cases). The experiments were conducted over a (corrected) gas temperature, T_{gas} , range from 370 °C to 505 °C.

Gas velocity was measured using an S-type pitot tube [36] (Perfect Prime PT6302) with a pressure transducer (Sensirion SDP810-250) and the (corrected) gas temperature measured by the thermocouple to account for the density of the gas. Flow

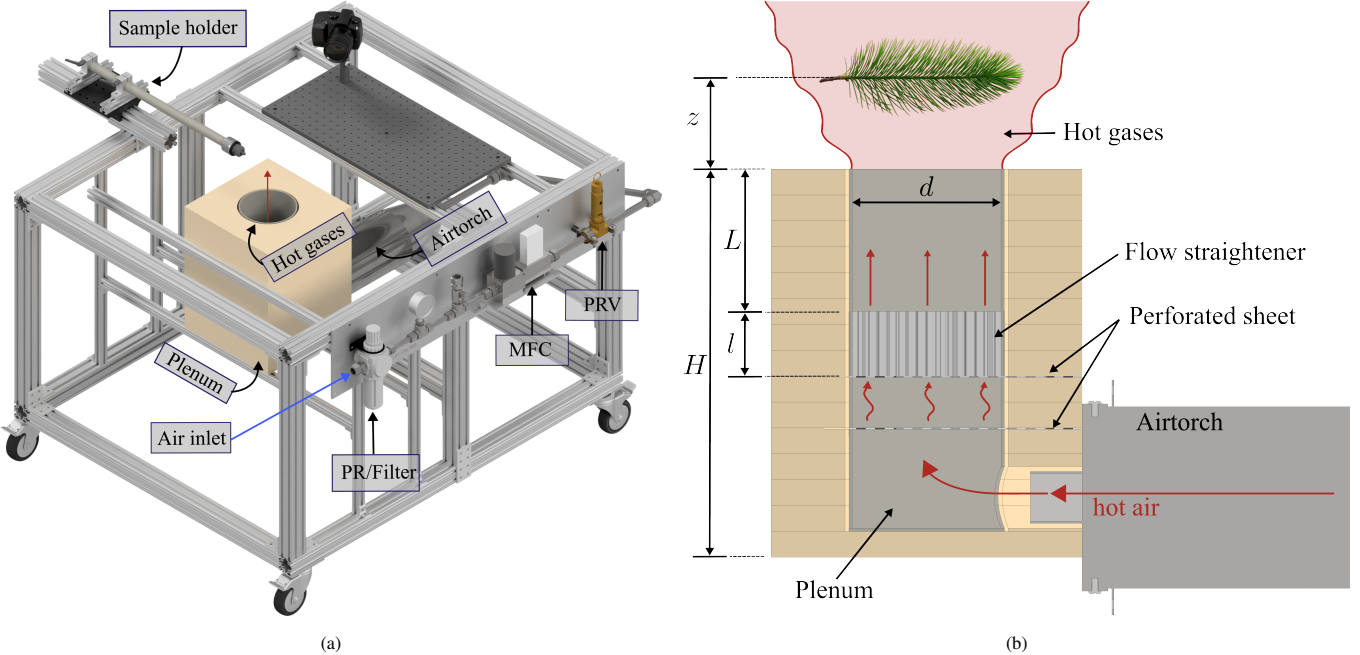


Figure 1: Experimental setup. (a) Isometric view of the 3D design featuring Convective Ignition Facility and its sub-systems. PR/Filter stands for pressure regulator and filter, MFC is the mass flow controller, and PRV is the (safety) pressure relief valve. (b) Lateral view illustrating the pathway of the hot gases from the airtorch through the flow conditioning plenum, culminating at the sample location situated atop the flow conditioning section at z . Note that the total height of the conditioning section is $H = 16''$ (406 mm).

velocity, v_{gas} , was calculated using an empirically calibrated S-type Pitot equation based on Bernoulli's principle:

$$v_{gas} = C(\Delta p) \sqrt{\frac{2\Delta p}{\rho(T_{gas})}} \quad (1)$$

Here, $C(\Delta p)$ is the empirical calibration coefficient of the S-type Pitot tube, Δp is the differential pressure measured by the pressure transducer (in Pa), and $\rho(T_{gas})$ is the gas density as a function of the gas temperature. The differential pressure provided by the sensor was corrected to account for pressure losses along the length and internal diameter of the connecting hoses, following the recommendations outlined in the Sensirion SDP Engineering Guide. The thermocouple junction was positioned adjacent to the inlet of the Pitot probe, with a lateral offset of approximately 6 mm from the sensing orifice to minimize flow disturbance. The S-type Pitot tube was calibrated in a mid-scale wind tunnel with a cross-sectional area of $0.8 \times 0.8 \text{ m}^2$ [37], from which the pressure-dependent calibration curve $C(\Delta p)$ was obtained. The calibration involved comparing the dynamic pressure readings obtained with the pitot tube and pressure transducer to the wind velocity measured using a Dantec Dynamics hot-wire anemometer (MiniCTA) at a 10 kHz sampling rate (which was calibrated on a separate setup with a mass flow controller and a tube long enough for fully-developed flow). The flow velocity was maintained constant throughout all experiments. To ensure this, velocity was measured in every case, allowing for necessary adjustments either to the set temperature on the PID controller of the airtorch or to the mass flow rate on the mass flow controller. The final recorded velocity across all cases was $v_{gas} = 2.41 \pm 0.09 \text{ m}\cdot\text{s}^{-1}$,

measured at the center of the sample location at z in Fig. 1b. A detailed description of the flow characterization procedure is provided in [Appendix A](#).

Both the thermocouple and the pressure transducer are connected to an Arduino UNO for data acquisition. The thermocouple is paired with its dedicated amplifier (Adafruit MAX31855), which is then interfaced with the Arduino. In contrast, the pressure transducer connects directly to the microcontroller. The data is acquired at a 4 Hz sampling rate and live plots are utilized to observe steady-state conditions during the experiment.

2.3. Ignition experiments

In the ignition experiments, a Douglas fir branch sample was placed on a sample holder (cf. Fig. 1a), which was then positioned above the flow outlet using a carriage system ("Sample holder" in Fig. 1a) to prevent preheating of the fuel. The time required to transfer the sample from ambient conditions to the hot convective flow at the testing location is less than one second. The moment the sample was positioned at the testing location in the hot convective flow marked the start of the experiment. Each experiment was recorded using a DSLR camera, and video analysis identified two key times: onset of glowing combustion, t_{glow} and time to flaming ignition, t_{ig} , and the flame height. Additionally, in a subset of experiments, a high-speed color camera (Edgertronic SC2+) was used to capture the onset of flaming ignition, triggered at the first sight of a luminous flame kernel. The average acquisition time was approximately 1.0 second (0.5 seconds pre-trigger and 0.5 seconds post-trigger), with a frame rate ranging from 3000 to 3500

fps.

To ensure the reliability and consistency of the results, each experiment was repeated three times for every gas temperature and fuel moisture content combination. The ignition outcome of an experiment was considered to be “Flaming Ignition” (FI)³⁰⁵ if a luminous flame formed and anchored to the Douglas fir sample. Alternatively, the ignition outcome was considered “No Ignition” (NI) if FI was not observed within 5 minutes or the sample experienced significant thermal degradation leading to it breaking. This 5-minute threshold was chosen because, beyond this duration, structural deformation (e.g., bending or breaking) was commonly observed, and visible pyrolysis gas emission typically ceased, making ignition unlikely and experimental conditions inconsistent. This allowed for the calculation of ignition probability and provided a robust dataset for subsequent analysis.³¹⁰ In all FI cases, glowing combustion (localized smoldering combustion resulting in visible incandescence) preceded flaming ignition, although some cases exhibiting glowing combustion did not result in FI. There were no observations of so-called “flashing ignition” where a gas phase flame would occur, but fail to propagate to fuel sample achieving a sustained ignition.

2.3.1. Fuel selection and conditioning

The selected fuel consisted of Douglas fir branches, each approximately 6 inches (15.2 cm) in length. An example of a sample branch is shown in Fig. 2a. These branches were harvested from a Douglas fir tree purchased from a tree farm and transported to the laboratory. Two drying methods were employed to prepare the samples: (1) natural drying of detached branches,³²⁰ where the tree was cut into smaller branches and stored in plastic boxes without lids under ambient conditions (20 °C and 50% relative humidity) to prevent condensation, and (2) forced drying of the intact tree (with branches attached) in an 8 × 8 × 8 ft³ compartment equipped with a convective heater. A total of 171³³⁵ branches were tested under convective heating conditions. Tests were first conducted on the day the tree was obtained (representing high fuel moisture content) and then on subsequent days, using both drying methods to obtain samples with varying moisture contents. The moisture content was determined using the oven-dry weight method, where the fuel moisture content (FMC) is given by [5]:³⁴⁰

$$FMC = \frac{W_{fr} - W_d}{W_d} \times 100\% \quad (2)$$

Here, W_{fr} and W_d represent the fresh weight and dry weight (in grams) of the sample, respectively. On each day of testing,³⁴⁵ samples were randomly selected from the branches prepared by both drying methods to obtain a fresh weight of approximately 5.0 g. The samples were then placed in a free convection oven at 60 °C for 24 hours. This drying protocol was based on previous findings that indicated an equilibrium moisture content was reached before 24 hours, ensuring that the samples were well dried to obtain W_d . It is noteworthy that, for each experiment, the authors endeavored to select branches that were as simi-

lar as possible; however, the intrinsic natural variation among specimens is unavoidable.

2.4. Thermogravimetric analysis

Thermogravimetric Analysis (TGA) was employed in this study to characterize the solid fuel thermal decomposition and determine associated kinetic parameters for an Arrhenius form of thermal degradation reactions in solid-phase wildland fuels (the activation energy, E_a , and pre-exponential factor, A). TGA involves measuring mass changes as samples undergo controlled heating, providing insights into thermal stability and decomposition kinetics. The equipment used was a TA Instruments Q50.

TGA was conducted on two different parts of the Douglas fir branches: the pine needle and the bark. The pyrolysis of both components was modeled using a unified set of pyrolysis kinetics, which will be shown from the TGA results that pine needles and bark exhibit similar thermal decomposition behavior under heating. While these woody fractions may differ in composition and devolatilization characteristics, this simplification reduces model complexity without substantially affecting heat release predictions [38]. The raw materials were ground into a fine powder and sieved using a sieve with an opening size of 5.0 μm. The small particle size minimizes heat and mass transfer effects, ensuring that temperature and composition throughout the sample can be approximated as uniform [39]. The initial sample mass was approximately 10 mg. The experimental temperature ranged from 20 °C to 700 °C, with samples heated at constant rates. To improve the reliability of the derived kinetic parameters, heating rates of 5, 10, 15, and 20 K·min⁻¹ were applied for each material.

Each TGA experiment was repeated three times. Additionally, experiments for each material were conducted under both inert and oxidizing environments, using nitrogen gas and air as the environmental gases, respectively. The flow rate of the gas entering the TGA furnace was maintained at 60 mL·min⁻¹.

3. Experimental Results and Discussion

3.1. Ignition behavior

In this study, ignition is defined as the moment of sustained flaming ignition of the Douglas fir samples exposed to convective heating. Flaming ignition behavior was observed to follow a consistent pattern, with glowing combustion always preceding flaming ignition in all cases. During the glowing phase, a red-orange glow was seen on the surface of the samples, which gradually transitioned to flaming ignition, as shown in Fig. 2.

3.1.1. Critical conditions for flaming ignition

An observed ignition probability was determined for each testing condition, with three repetitions conducted at each gas temperature. Considering all the data (regardless of fuel moisture content) a logistic regression was applied to the binary ignition outcome data, as depicted in Fig. 3, following approaches used in previous ignition studies [40, 41]. The resulting probability distribution is shown in Fig. 3, where each navy-blue diamond marker represents the observed ignition probability based on

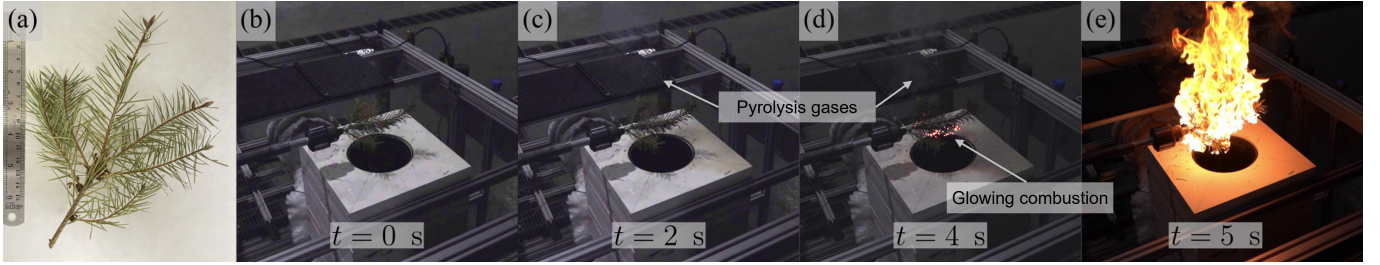


Figure 2: Sequential observations of the transition from glowing combustion to flaming autoignition in Douglas fir samples under convective heating at a gas temperature of 480°C . (a) The sample was cut from the main tree. (b) It was placed on the sample holder and positioned above the flow outlet, initiating convective heating at $t = 0$ s. (c) Pyrolysis gases began to release from the sample. (d) Glowing combustion appeared alongside the continued release of pyrolysis gases. (e) Finally, flaming autoignition occurred.

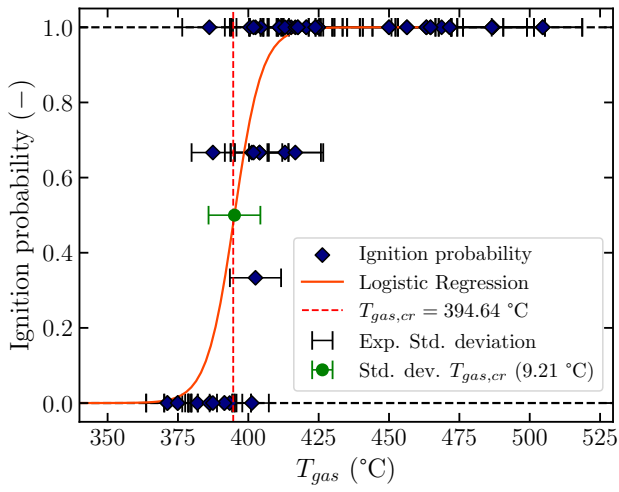


Figure 3: Logistic regression of ignition probability versus gas temperature. The red curve shows the logistic regression; blue diamonds indicate observed ignition probabilities with error bars reflecting the standard deviation of the gas temperatures. The critical gas temperature for 50% ignition probability is $T_{\text{gas},\text{cr}} = 394.64^{\circ}\text{C}$, with a corresponding variation shown by the green error bar.

the three repetitions at a given gas temperature. Horizontal error bars indicate the standard deviation of gas temperature measurements. The critical gas temperature, defined as the temperature at which the logistic regression predicts a 50% ignition probability, is marked by the vertical dashed red line and was determined to be $T_{\text{gas},\text{cr}} \approx 395^{\circ}\text{C}$. To evaluate the influence of fuel moisture content (FMC), separate logistic regressions were performed for each FMC level using the same dataset. This analysis yielded multiple logistic regression curves, revealing that the critical gas temperature varies slightly with FMC. This variation (one standard deviation) is represented by the green horizontal error bar at the green circle marker in Fig. 3, illustrating the variation of the critical gas temperature for FMC values ranging from ~ 0 to 90% .

The critical gas temperatures corresponding to the tested FMC levels were extracted and plotted in Fig. 4 as light blue diamonds. The dashed light blue curve was manually drawn to approximate the boundary representing a 50% ignition probability across all FMC values, serving as a visual representation

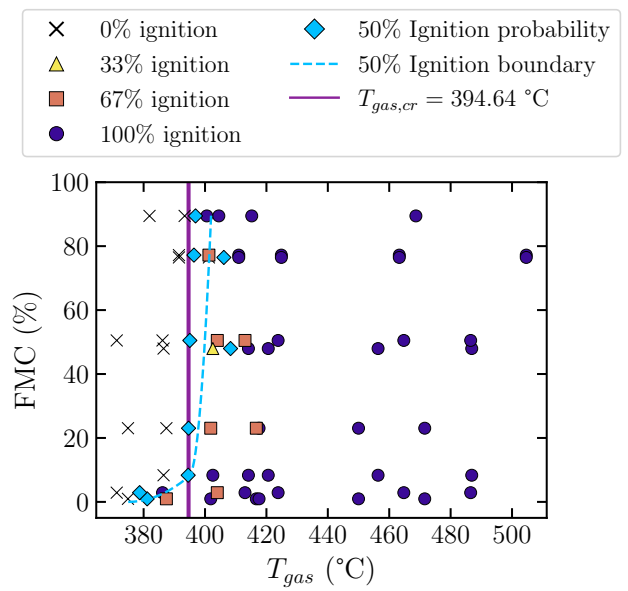


Figure 4: Distribution of ignition probability as a function of gas temperature and fuel moisture content (FMC), with light blue diamonds representing the critical gas temperatures, $T_{\text{gas},\text{cr}}$, for each experimental FMC value, obtained from logistic regression analysis. A dashed light blue line approximates the 50% ignition probability boundary across all FMC values.

of the ignition boundary. This graph illustrates the distribution of the observed ignition probability for each experimental condition and corresponding fuel moisture content (FMC). The ‘x’ markers indicate cases where ignition did not occur, while the markers represent ignition probabilities of $1/3$ (yellow triangle), $2/3$ (orange square), and $3/3$ (blue circle). The critical gas temperature, considering all FMC values (cf. Fig. 3), is shown as a vertical solid purple line.

Figures 3 and 4 collectively demonstrate that ignition probability transitions from 100% to 0% across the critical conditions. Additionally, as discussed in Section 3.1.2, the time required for flaming ignition increases as the gas temperature approaches the critical threshold. Notably, ignition observations indicate that at lower FMC values ($FMC \leq 5\%$), ignition can still occur below the critical gas temperature (see Fig. 4).

3.1.2. Time to ignition (experiments)

The ignition delay times were measured and plotted against the gas temperature in Fig. 5a. Higher gas temperatures tended to have low ignition times. As the gas temperature decreases, the ignition time increases until the ignition probability is no longer 100% and then ignition is not achieved. The trend is analogous to that for the ignition time of samples from radiative heating [42–45].

390
395

nition and the onset of glowing combustion, $\Delta t = t_{ig} - t_{glow}$, is further analyzed in Fig. 5b, where lower gas temperatures correspond to longer Δt . Specifically, for $T_{gas} \geq 450$ °C, $\Delta t = 5.0 \pm 2.5$ s, whereas below this threshold, Δt increased to 10.8 ± 10.9 s—over two times greater with individual ignition times up to approximately four times greater. Notably, in the lower temperature range, the standard deviation of Δt was considerably larger, approximately 4.4 times higher than in the high-temperature cases. This increased variability, along with the extended glowing phase duration, Δt , is attributed to the complexities and proximity to critical ignition conditions, where gas-phase reactions and their interactions with the solid phase become more pronounced [46].

Statistical analysis reveals that for $T_{gas} < 440$ °C, ignition delay times exhibit greater variability at higher FMC and are more consistent at lower FMC. The median FMC for these cases was 23%. A t-test comparing high and low FMC groups based on this median yielded a p – value of 0.024, indicating a statistically significant difference in ignition delay times between the groups. This suggests that FMC impacts ignition delay time under these conditions, with the observed difference unlikely to be due to random variation.

Furthermore, at temperatures below the critical gas temperature, the needles were observed to char, and ignition either did not occur or the branches fractured due to thermal degradation during the experiments. For cases near the critical gas temperature, ignition delay times were likely governed by the diffusion of oxygen into the vaporized fuel and the hot, charred surface, where gas-phase reactions played a dominant role, as discussed by Martin [47]. At higher gas temperatures, where the convective heat flux is greater, it is hypothesized that ignition delay times were primarily controlled by thermal diffusion (conduction) into the solid phase, as sufficient heat was rapidly conducted to initiate solid-phase reactions [16]. These distinctions in ignition mechanisms will be further explored and discussed in the thermal model (cf. Section 3.1.3) and numerical model (cf. Section 4).

3.1.3. Thermally controlled ignition model

A simplified transient heat transfer model was developed to better understand the ignition phenomenon. This model is developed applying conservation of energy to a cylindrical element, representing a single Douglas fir “pine needle” assuming the needle exhibits thermally thin behavior. The element is subjected to convective cross-flow heating along its circumference and experiences radiation losses to the cold walls of the room. Furthermore, radiative heating from the metallic plenum walls is incorporated into the model using view factor analysis. The resulting equation is a non-linear ordinary differential equation given by:

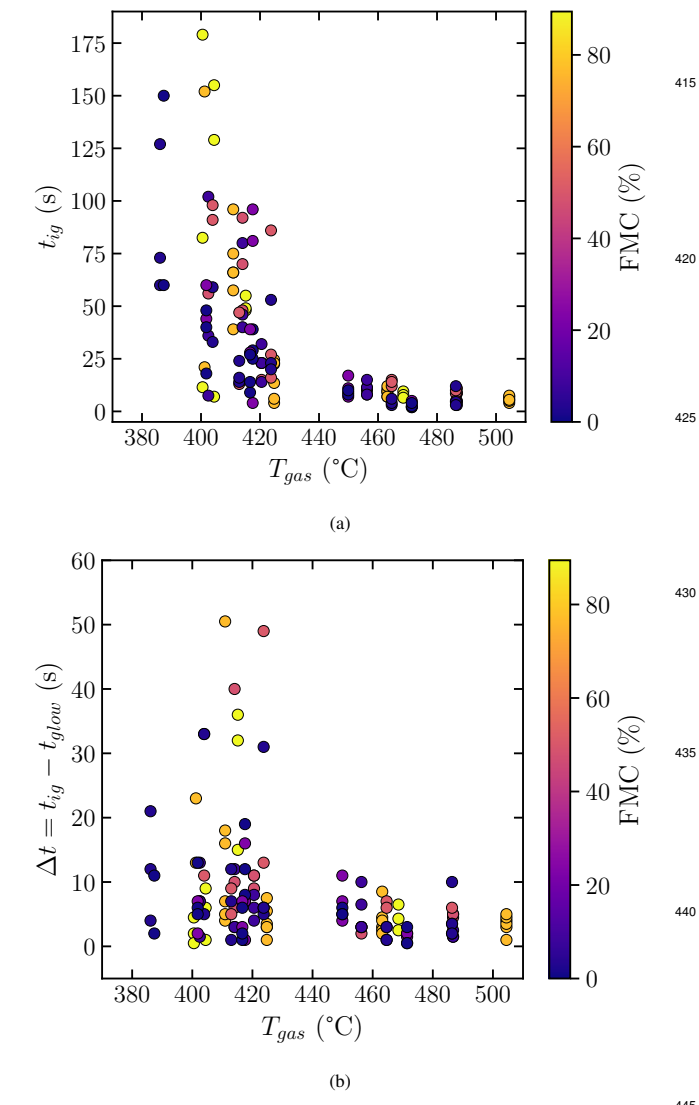


Figure 5: Impact of gas temperature and fuel moisture content (FMC) on ignition delay times. (a) Ignition delay times, t_{ig} , as a function of gas temperature, T_{gas} . (b) Difference between ignition and glowing times, $\Delta t = t_{ig} - t_{glow}$, versus gas temperature.

At high gas temperatures ($T_{gas} \geq 450$ °C), ignition occurred rapidly, with $t_{ig} = 7.8 \pm 3.6$ seconds. As the gas temperature approached the critical ignition threshold ($T_{gas} \approx 400$ °C), glowing combustion persisted but with notable changes. Both the duration of the glowing phase and the ignition delay times increased. The duration of the glowing phase extended, and ignition delay times became significantly longer. This delay, quantified as the difference between the onset of flaming ig-

450
400

$$(\rho c_p D)_k \frac{dT_s}{dt} = \dot{q}_{conv}'' + \dot{q}_{rad}'' - \dot{q}_{re-rad}'' \quad (3)$$

Or,

$$(\rho c_p D)_k \frac{dT_s}{dt} = \frac{\overline{\text{Nu}} k_{\text{gas}}}{D_k} (T_{\text{gas}} - T_s) + \varepsilon_m \sigma T_m^4 (F_{dA \rightarrow fs} + F_{dA \rightarrow cyl}) - \varepsilon_k \sigma (T_s^4 - T_\infty^4). \quad (4)$$

The temperatures of the pine needle, hot gases, metal surfaces of the plenum and ambient air are denoted by T_s , T_{gas} , T_m , and T_∞ , respectively. The density and specific heat capacity of the pine needle, subscript k , are represented by ρ_k ($\text{kg}\cdot\text{m}^{-3}$) and $c_{p,k}$ ($\text{J}\cdot\text{kg}^{-1}\cdot\text{K}^{-1}$). Additionally, ε_k is the emissivity (-), and σ is the Stefan-Boltzmann constant. The convective heat transfer coefficient, $\bar{h} = \overline{\text{Nu}} k_{\text{gas}} / D_k$, is calculated using the average Nusselt number $\overline{\text{Nu}}$, which was estimated using Whitaker's correlation for a cylinder in cross-flow [48]. Gas properties were evaluated at the film temperature, which is the average between the gas temperature and the pine needle temperature. The diameter D_k was measured from over 50 specimens, yielding an average value of $D_k = 0.75$ mm, which was used in the model. The radiative heat flux contribution from the metal surfaces, \dot{q}_{rad}'' , is determined theoretically by evaluating the thermal radiant energy exchange between the metal surfaces and a small differential disk element, dA , of diameter D_k , representing a patch of the Douglas fir needle. Two geometries are considered in the analysis: a disk, fs , representing the upper surface of the flow straightener with diameter d , and a coaxial cylindrical section, cyl , extending vertically from this disk to the end of the plenum, with height L . These geometries and their relative positions are illustrated in Fig. 1b. Radiative exchange is thus evaluated using view factors from the differential element dA to these two surfaces, denoted as $F_{dA \rightarrow fs}$ (to the disk surface of the flow straightener) and $F_{dA \rightarrow cyl}$ (to the cylindrical walls of diameter d and height L), respectively (cf. Fig. 1b). It should be noted that, because the flow straightener consists of an array of carbon-steel tubes, its actual exposed surface area is significantly smaller than that of a solid disk with diameter d , corresponding to the cylindrical plenum. Specifically, the effective radiating area is 44.14% of the total area of such a disk. This reduction factor was applied to adjust the view factor $F_{dA \rightarrow fs}$ accordingly. Analytical expressions for both view factors are available in Refs. [49, 50]. The view factor from the differential disk element to the inner surface of the cylinder was obtained using the reciprocity relation for view factors [51], as the available analytical expression corresponds to the inverse configuration [50]. For simplicity, it is assumed that the metal walls have a temperature approximately equal to the gas temperature ($T_m \approx T_{\text{gas}}$), and the emissivity of the metal surfaces, ε_m , is modeled as a step-wise function of temperature based on the findings from Ref. [52]. The solid properties were obtained from the literature, with $\rho_k = 514 \text{ kg}\cdot\text{m}^{-3}$ [53] and $c_{p,k} = 1800 \text{ J}\cdot\text{kg}^{-1}\cdot\text{K}^{-1}$ [44]. For the spectral properties, an emissivity of $\varepsilon_k = 0.699$ was used [44]. The model was numerically integrated using the 4th-order Runge-Kutta method [54]. The model results are shown in Fig. 6. As observed, at lower gas temperatures, ignition delays are long due

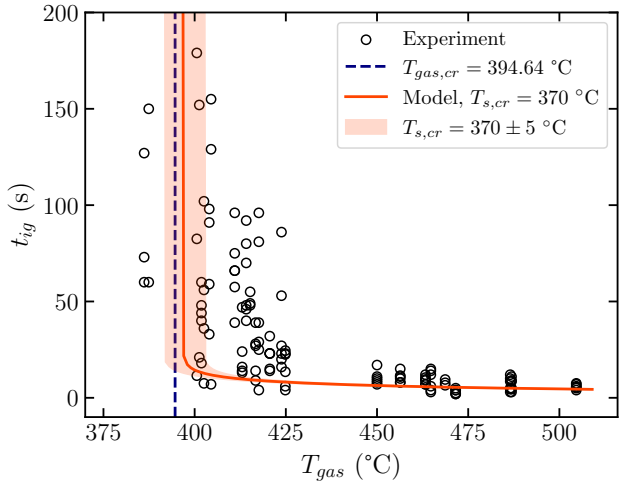


Figure 6: Predicted ignition delay times for a critical solid temperature of $T_{s,cr} = 370 \pm 5^\circ\text{C}$ compared with experimental data.

to the limited net heat flux to the sample. Although radiative input from the apparatus walls remains constant, the convective contribution decreases as the solid temperature of the sample, T_s , warms, while radiative losses increase with T_s^4 , resulting in slower heating rates. At higher gas temperatures, the convective flux remains significant throughout the heating process, and ignition occurs more rapidly. At the highest gas temperature tested ($T_{\text{gas}} = 504.6^\circ\text{C}$), at the start of exposure, when the sample remains near ambient temperature ($T_s = T_\infty = 20^\circ\text{C}$), convective heat fluxes peak at approximately $95 \text{ kW}\cdot\text{m}^{-2}$ ($\bar{h} \approx 195 \text{ W}\cdot\text{m}^{-2}\cdot\text{K}^{-1}$), subsequently decreasing as the surface heats, and approaching $22 \text{ kW}\cdot\text{m}^{-2}$ by the time corresponding to the average ignition delay around that gas temperature, while incident radiation from the walls to the sample remains constant at around $4.6 \text{ kW}\cdot\text{m}^{-2}$. These results highlight the dominant role of convection in this configuration, particularly during the early heating period, and confirm that radiative contributions, although present, are secondary in comparison with convective heating in terms of ignition effectiveness. A critical solid temperature of $T_{s,cr} = 370 \pm 5^\circ\text{C}$ was chosen as a hypothetical ignition temperature of the Douglas fir needles. This value provides approximate agreement with the experimentally derived critical gas temperature, $T_{\text{gas},cr} \approx 395^\circ\text{C}$, and offers a physically reasonable basis for comparing predicted ignition delays with observed behavior. Regarding the prediction of ignition delay time, the model shows good agreement with the experimental data at high gas temperatures (when $T_{\text{gas}} \geq 450^\circ\text{C}$), where ignition delay is largely governed by the pyrolysis time. As conditions approach the critical threshold for ignition, variability increases and gas-phase reaction dynamics become more influential [46]; while the simplified thermal model does not explicitly resolve these chemical processes, it still captures the general trend and provides reasonable estimates of ignition delays under these low-flux conditions.

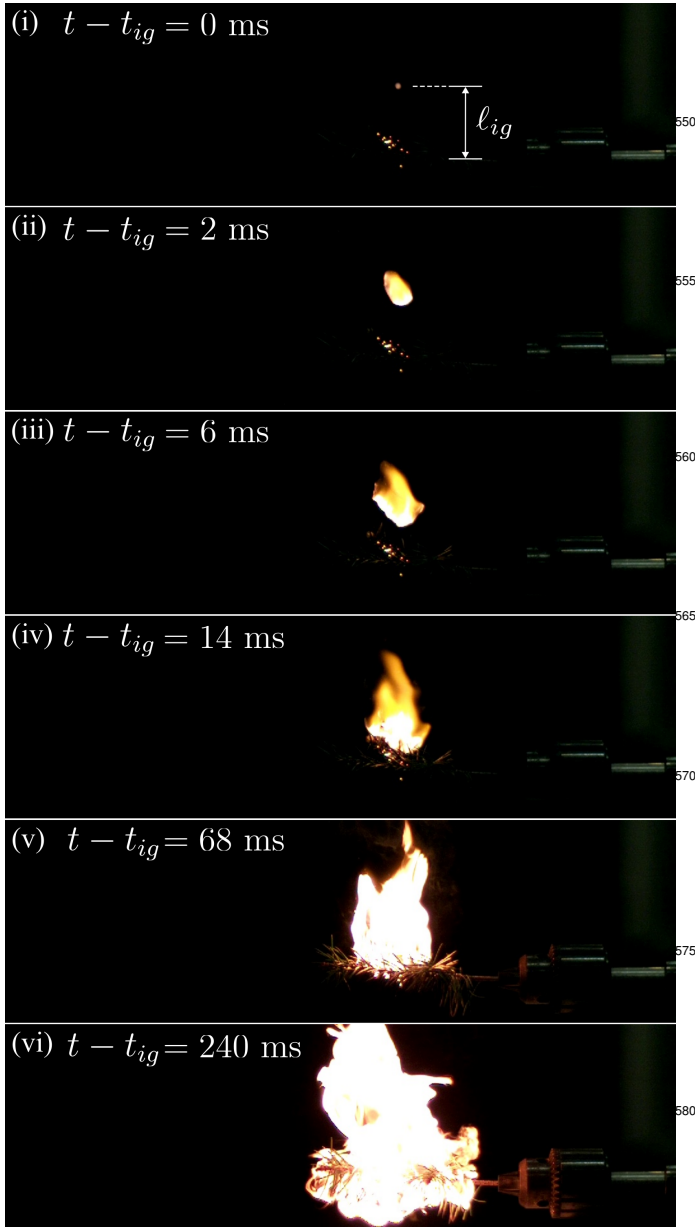


Figure 7: Evolution of gas-phase ignition. From top to bottom: ignition location₅₈₅ (ℓ_{ig}), flame propagation, and subsequent fuel ignition. For this case: $T_{gas} = 463.16^\circ\text{C}$, $\ell_{ig} = 5.48 \text{ cm}$ and $v_f = 3.91 \text{ m}\cdot\text{s}^{-1}$. Panel (i): gas-phase ignition and its location, ℓ_{ig} , above the sample, Panels (ii - v): flame propagation to the fuel surface, Panel (vi): heat feedback from flame intensifies burning. Times after t_{ig} listed have an uncertainty of $\pm 0.5 \text{ s}$ due to imperfect synchronization of the DSLR and high speed cameras.

which includes a series of frames depicting the ignition point, flame propagation, and subsequent solid fuel ignition. The ignition location and gas-phase flame speed were determined from high-speed camera recordings of each experiment using OpenCV in Python. Video analysis was possible for 25 out of the 27 downstream flaming ignition cases. In the remaining two cases, ignition occurred outside the camera field of view, preventing determination of the ignition location or flame propagation.

Figure 8a illustrates the relationship between the downstream ignition length, ℓ_{ig} , and the gas temperature. Here, ℓ_{ig} is defined as the vertical distance from the horizontal centerline of the sample, aligned with the direction of flow. Similarly, Fig. 8b shows the relationship between the vertical gas-phase flame propagation speed, v_f , and the gas temperature. The process for determining ℓ_{ig} and v_f is demonstrated using the images in Fig. 7. Panel (i) of Fig. 7, at $t - t_{ig} = 0$, shows the onset of gas-phase ignition, and the downstream ignition length, ℓ_{ig} , which is found to be 5.48 cm in the case shown. The gas-phase flame speed, v_f , was determined as the net speed of flame propagation along the downstream ignition length, expressed as $v_f = \ell_{ig}/\Delta t_{prop}$, where Δt_{prop} is the propagation time from the onset of gas-phase ignition until the flame makes contact with the solid fuel. As shown in Panels (i)–(iv) of Fig. 7, this flame propagation occurred over $\Delta t_{prop} = 14 \text{ ms}$ (the elapsed time between Panels (i) and (iv)), resulting in a flame speed of $v_f = 3.91 \text{ m}\cdot\text{s}^{-1}$.

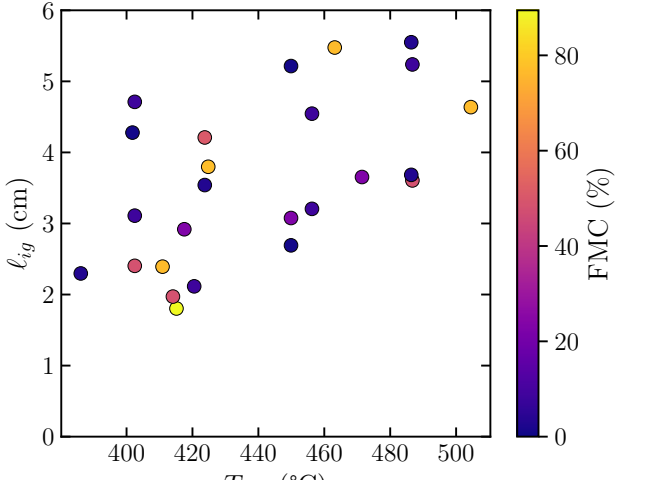
A clear trend of the downstream ignition length or the flame propagation speed is not observed. There is perhaps a slight increase in ℓ_{ig} and v_f with respect to the gas temperature, but this increase is similar in magnitude to the variation exhibited between the tests at the same gas temperature. This might be a result of the small number of ignition observations displaying this phenomena. A study on the ignition of wooden dowel rods by convective heating at higher temperatures found that downstream gas-phase ignition occurred at a gas temperature of 600°C , while at 800°C , gas-phase ignition was observed closer to the fuel surface [26]. Given this differences between this work and the previously cited study, this suggests that fuel characteristics (e.g., composition, morphology) may play a role, with their influence becoming more pronounced over larger gas temperature ranges. Notably, most of the downstream ignition events in this study occurred at relatively low FMC (< 30%), with the median FMC for these cases being 15.7%, and the 25th and 75th percentiles were found to be 4.3% and 47.9%, respectively. This suggests that FMC may indeed be a contributing factor to the observed ignition behavior.

3.1.4. Location of gas-phase ignition

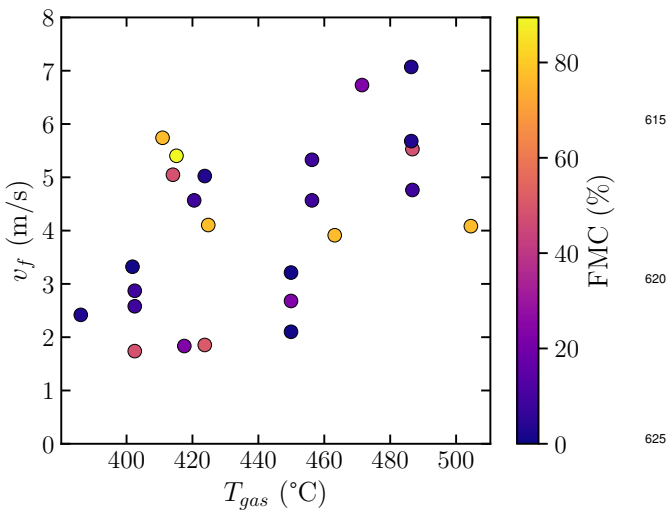
The location of gas-phase flaming ignition was not consistent for all tests. In most (100 out of 171 experiments) tests resulting in flaming ignition, gas-phase flaming ignition occurred near the fuel sample. However, in only 27 experiments (spanning full range of gas temperatures), gas-phase ignition occurred at a substantial distance downstream (>1 cm above) from the solid fuel surface. Similar behavior was observed by others studying the convective ignition of wooden dowel rods [26]. The evolution of a downstream gas-phase ignition is shown in Fig. 7,

3.1.5. Flame heights

After ignition occurred in the experiments, the flames grew substantially as heat feedback from the flame to the solid fuel became established. The peak flame height, L_f , was measured from the DSLR video recordings of each experiment using OpenCV in Python. For recordings at 60 fps, the maximum flame height from the video frames of each experiment was identified and recorded. The results are presented in Fig. 9. As



(a)



(b)

Figure 8: High-speed camera results for downstream gas-phase ignition cases:⁶³⁰ (a) Downstream ignition distance, ℓ_{ig} , vs gas temperature T_{gas} , and (b) average flame propagation speed, v_f , vs gas temperature from the gas-phase towards the solid fuel sample.

shown in Fig. 9, there is a clear trend: as the ignition delay time ⁶³⁵ decreases, the flame height increases. Higher gas temperatures reduce ignition delay times and accelerate pyrolysis, leading to greater release of flammable gases and more intense combustion. The resulting taller flames enhance radiative heat transfer to the fuel bed, further promoting pyrolysis and sustaining the ⁶⁴⁰ combustion process.

To analyze the relationships influencing peak flame height, an ⁶⁴⁵ Ordinary Least Squares (OLS) regression was applied. The regression equation can be represented as follows:

$$L_f = \gamma_0 + \gamma_1 FMC + \gamma_2 T_{gas} + \gamma_3 t_{ig} + \xi \quad (5)$$

In this equation, γ_0 is the intercept, while γ_1 , γ_2 , and γ_3 are the coefficients for fuel moisture content (FMC), gas tempera-

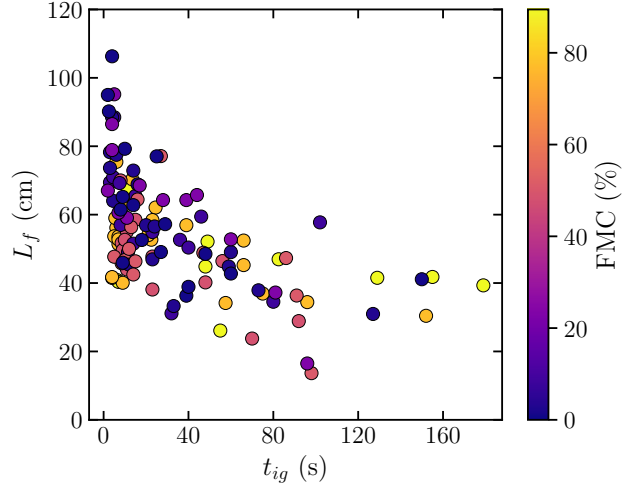


Figure 9: Peak flame height L_f versus ignition delay time (t_{ig}), with fuel moisture content (FMC) represented by the color scale for both cases.

ture, T_{gas} , and ignition delay time, t_{ig} , respectively. The term ξ represents the error term (residuals), where the average error was $|\xi| = 10.4$ cm. Although FMC influences ignition delay time, this relationship is weak in the context of the Ordinary Least Squares (OLS) model. The correlation coefficient of 0.13 between FMC and t_{ig} indicates low linear dependence, further supported by Variance Inflation Factor (VIF) values below 2 for all predictors. This confirms that multicollinearity is not a concern, ensuring each predictor contributes independently to the model without inflating standard errors. The regression analysis yielded several insights. The coefficient for FMC, $\gamma_1 = -0.123$, indicates the change in peak flame height, L_f , for a one-unit increase in FMC, holding other variables constant. This implies that for each 1% increase in FMC, peak flame height decreases by approximately 0.123 cm, with a total difference of approximately 11 cm over the entire range of FMC, which is statistically significant (p -value = 0.0013). The reduction in peak flame height (~ 10.89 cm) corresponds to roughly 80% of the smallest peak flame heights measured and about 10% of the largest.

Additionally, the coefficient for gas temperature ($\gamma_2 = 0.0474$) indicates that for each 1 °C increase in T_{gas} , the average flame height increases by approximately 0.0474 cm. This change is not statistically significant (p -value = 0.315), and over the observed range of gas temperatures (from 386 °C to 504 °C), corresponds to a total effect of approximately 5.6 cm. This positive relationship suggests that higher gas temperatures are associated with slightly taller flames, but the effect is relatively small compared to other variables, such as fuel moisture content.

Finally, the coefficient for ignition delay time ($\gamma_3 = -0.202$) indicates that for each 1-second increase in t_{ig} , the average flame height decreases by approximately 0.202 cm. This change is statistically significant (p -value = 4.8×10^{-6}) and, over the observed range of ignition delay times (from 2.0 to 179 seconds),

corresponds to a total effect of approximately 36 cm. This negative relationship suggests that longer ignition delay times may lead to shorter flames, possibly due to slower burning processes associated with wetter or less flammable conditions, or more complete thermal degradation of the sample prior to ignition.

3.2. Thermogravimetric analysis

Thermal degradation plays a crucial role in the pyrolysis and ignition process, and thermogravimetric analysis can be used to characterize material decomposition under controlled heating. Kinetic parameters from the thermogravimetric analysis will be incorporated into the numerical simulation to model pyrolysis kinetic parameters including activation energy and pre-exponential factors (see Section 4 for details). The thermal degradation of the material was modeled by the mass loss conversion degree, α . This conversion degree at a given time t was calculated using the initial mass m_i , the final residual mass m_f , and the mass at time t , m_t , as $\alpha = (m_i - m_t)/(m_i - m_f)$. The reaction is influenced by a pre-exponential factor, A , an Arrhenius-like term related to temperature T , and an apparent activation energy, E_a .

The linear isoconversional method, as developed by Kissinger-Akahira-Sunose (KAS) [55], was used to analyze the thermal degradation process for a given conversion degree α and heating rate. The method is expressed as:

$$\ln\left(\frac{\beta}{T^2}\right) = \ln\left(\frac{AR}{E_{ag}(\alpha)}\right) - \frac{E_a}{RT} \quad (6)$$

Here, β represents the heating rate, and R is the universal gas constant. For a first-order reaction, integrating the equation while assuming the initial temperature and conversion degree to be zero gives the integral form of the reaction model, defined as $g(\alpha) = -\ln(1 - \alpha)$. By plotting $\ln(\beta/T^2)$ as a function of $-1/T$ for various heating rates, the activation energy can be determined from the slope of the linear relationship at each given conversion degree. Furthermore, once the activation energy is obtained, the pre-exponential factor can be calculated using the corresponding linear equation, where b is the intercept of the linear fitted line:

$$A = \frac{E_a \exp(b)g(\alpha)}{R} \quad (7)$$

The KAS method is employed to determine activation energy and is one of several techniques used to estimate kinetic coefficients. While model-based approaches assume potential kinetic reactions during pyrolysis and derive kinetic coefficients through inverse methods, identifying the exact mechanisms is complex and beyond the scope of this study. For detailed descriptions, refer to Ref. [56]. In contrast, model-free methods, such as the KAS method, do not require calculating apparent energy for each conversion degree. The KAS method offers the advantage of estimating model-free coefficients across multiple conversion degrees, enabling a comprehensive fit for the pyrolysis process without requiring detailed mechanistic assumptions [55].

Figure 10 illustrates the variation of activation energy, E_a , and the pre-exponential factor, A , with the conversion degree, α , for pine needles and bark in nitrogen and air environments. In both samples, both E_a and A vary with α , highlighting the complexity of the decomposition process. For the pine needles sample in N_2 (cf. Fig. 10a), the activation energy increases up to approximately 60 kJ·mol⁻¹ at $\alpha \approx 0.35$. Similarly, for the bark sample in N_2 (cf. Fig. 10b), E_a initially rises sharply, peaking at around 50 kJ·mol⁻¹ near $\alpha = 0.3$. This behavior suggests that at lower conversions, the decomposition is primarily governed by more thermally resistant components, such as cellulose or lignin, which require higher energy input for degradation due to their complex structures and strong chemical bonds [57]. For both pine needles and bark in N_2 , E_a remains relatively constant until $\alpha \approx 0.7$, after which a secondary rise occurs toward the end of the process, indicating the presence of secondary reactions, possibly associated with char formation. This increase is more pronounced in the pine needles sample, where both E_a and A peak higher than in the bark sample. This difference in activation energy between the bark and pine needles in N_2 environment is likely due to the structural and compositional differences between the two biomasses. The lower E_a values for bark may suggest a higher proportion of volatile components, such as hemicellulose, which decompose at lower temperatures compared to the more recalcitrant, lignin-rich bark.

For both samples in the N_2 environment, the pre-exponential factor, A , exhibits a trend similar to that of E_a , suggesting a consistent decomposition mechanism throughout the conversion range. For the pine needles in the N_2 environment (cf. Fig. 10a), the pre-exponential factor, A , exhibits a peak around $\alpha = 0.35$, with a slightly higher maximum value than that of the bark sample. This suggests that pine needles have overall higher reactivity, likely due to a greater proportion of easily degradable components that degrade more rapidly at lower energy inputs. For the bark sample in N_2 (cf. Fig. 10b), A peaks at $\alpha \approx 0.3$, reaching values around 10^9 s⁻¹ before decreasing and rising again at higher conversion levels ($\alpha \approx 0.75$). The high values of A during the early stages of decomposition suggest a rapid reaction rate, corresponding to a quick release of volatiles, as described by chemical kinetic equations. The activation energies and pre-exponential factors for both samples in N_2 exhibit similar general trends, with pine needles having slightly higher activation energies for decomposition, particularly during the early stages of the reaction. This difference is likely attributed to the more complex and recalcitrant structure of bark, which contains a higher proportion of lignin, compared to the more cellulose-rich pine needles [58].

In the air environment (cf. Figs. 10c and 10d), the behavior of both E_a and A is less pronounced in terms of peaks and fluctuations compared to the nitrogen environment. Another feature is the decrease in E_a around $\alpha \approx 0.7$ for both bark and pine needles, indicating that decomposition becomes progressively easier as the material burns off in the presence of oxygen. Moreover, A decreases substantially as E_a decreases. This trend contrasts with the nitrogen environment, where E_a fluctuates more dynamically with α throughout the conversion process.

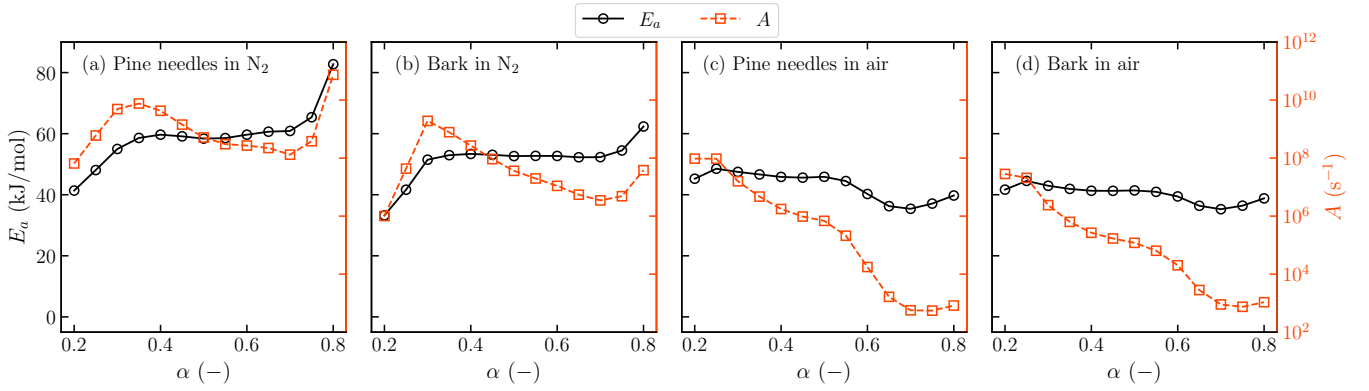


Figure 10: Activation energy and pre-exponential coefficient against different conversion degrees, α , of (a) pine needles in N_2 , (b) bark in N_2 , (c) pine needles in air, and (d) bark in air.

For the pine needles in the air environment (cf. Fig. 10c), the activation energy starts at around $45 \text{ kJ}\cdot\text{mol}^{-1}$, then quickly increases to around $48 \text{ kJ}\cdot\text{mol}^{-1}$, before decreasing slightly and remaining constant at approximately $45 \text{ kJ}\cdot\text{mol}^{-1}$ until $\alpha = 0.65$. Beyond this point, E_a begins to decrease and then increases again at $\alpha \approx 0.75$. For the bark sample in the air environment (cf. Fig. 10d), the activation energy starts at around $40 \text{ kJ}\cdot\text{mol}^{-1}$, quickly peaks to around $44 \text{ kJ}\cdot\text{mol}^{-1}$, and then decreases slightly and remains constant at about $41 \text{ kJ}\cdot\text{mol}^{-1}$ until $\alpha \approx 0.65$. Beyond this point, E_a decreases and then increases again toward the end of the conversion. This behavior is similar to that observed for the pine needles in the air environment. The decrease in E_a at higher α suggests that oxidative reactions in the presence of air reduce the energy barrier for decomposition as volatiles and char form. Compared to the nitrogen environment, where E_a peaked around $50 \text{ kJ}\cdot\text{mol}^{-1}$ at $\alpha \approx 0.30$, the air environment lowers the activation energy barrier due to the active role of oxygen in accelerating decomposition.

For the pine needles in the air environment 10c), the pre-exponential factor starts at around 10^8 s^{-1} and then consistently decreases throughout the conversion process. This suggests a lower reaction rate. For the bark in the air environment (cf. Fig. 10d), the pre-exponential factor starts at around 10^7 s^{-1} and decreases steadily until $\alpha \approx 0.6$, reaching a final value of nearly 10^3 s^{-1} . This decrease indicates that, in the air, the reaction rate slows as decomposition advances, likely due to the depletion of easily oxidizable compounds and the formation of more stable char. Overall, both pine needles and bark show a decrease in the pre-exponential factor in the air environment, which reflects a shift in the reaction dynamics due to oxidative decomposition. Finally, additional TGA results and kinetic analysis details are provided in Appendix B for completeness.

4. Numerical simulation

4.1. Descriptions of the simulation

To better understand the ignition phenomena, the experiment is modeled using the Fire Dynamics Simulator (FDS, version 6.9.1), a three-dimensional, time-dependent computational

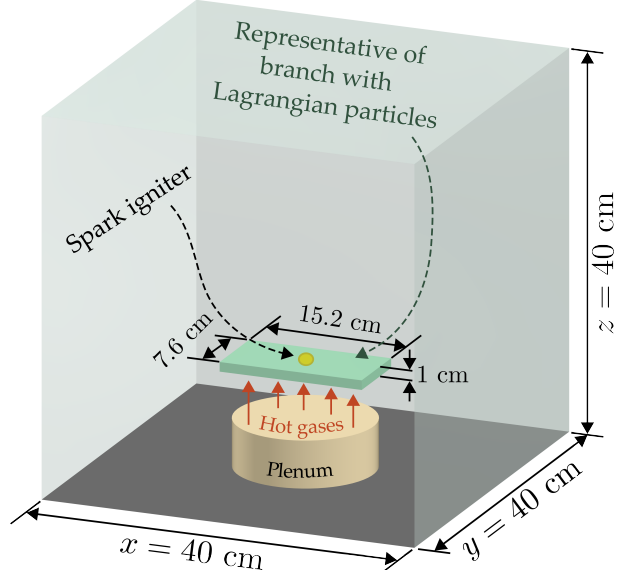


Figure 11: Computational domain to scale; open boundary conditions on all faces except the floor.

fluid dynamics (CFD) solver designed for low-Mach number flows involving combustion processes [59]. Turbulence is modeled using large eddy simulation (LES) with Deardorff's subgrid eddy viscosity model. Radiative heat transfer is handled via the radiation transport equation, assuming a non-scattering gray gas.

The pine branch used in the experimental setup is modeled as discrete, fixed-position Lagrangian particles. Convective heat transfer from the airflow to the particles is computed using empirical correlations for flow around cylinders, while radiative heat transfer is modeled by assuming the particles behave as optically gray bodies ($\varepsilon = 0.9$). As these particles experience both convective and radiative heat transfer, their temperature rises, initiating processes such as moisture evaporation, pyrolysis, and char oxidation. Radiation primarily serves as the main mechanism of heat loss prior to ignition. Figure 11 illustrates the computational domain used for the simulations. The do-

main measures $40\text{ cm} \times 40\text{ cm} \times 40\text{ cm}$, with a uniform mesh size of 6.25 mm. It fully encompasses the pine branch sample and the surrounding flow field. Open boundary conditions are imposed on all external faces, except the floor at $z = 0\text{ cm}$, to allow unimpeded flow and prevent artificial reflections.

The flow conditioning system (plenum of the CIF) is represented by a central cylindrical obstruction (5 cm tall), corresponding to the outlet plenum shown in Fig. 1b. An immersed boundary condition is applied to the cylinder, with its side-walls treated as inert, adiabatic, and non-slip surfaces. The top surface of the cylinder serves as the outlet, where fixed velocity and temperature boundary conditions replicate experimental conditions. No physical sample holder is included in the simulation for simplicity.

The pine branch is modeled as a rectangular volume of cylindrical Lagrangian particles, positioned directly above the plenum outlet. The vertical distance from the top surface of the plenum to the center of the rectangular particle volume is $z = 2.5\text{ in}$ (63.5 mm), which is 1 inch lower than the experimental setup to capture the effect of branch charring and mechanical integrity loss (cf. Fig. 1b). Particle dimensions are based on experimental measurements, accounting for variations between trials. Each particle has a length of 5 cm, and a surface-to-volume ratio (SVR) of $3,940\text{ m}^{-1}$. Given the relatively small size of the branch compared to the overall domain, this geometric simplification is not expected to significantly impact simulation accuracy. The rectangular region containing the particles has a total volume of approximately $1.162 \times 10^{-4}\text{ m}^3$ and includes 1,200 cylindrical Lagrangian particles. Based on the specified SVR, this corresponds to a particle diameter of approximately 1.03 mm. With a solid density of $514\text{ kg}\cdot\text{m}^{-3}$ [53], the total dry mass of the particle ensemble is approximately 25.4 g, yielding a bulk density of $218.7\text{ kg}\cdot\text{m}^{-3}$.

Combustion is modeled by assuming pyrolysis gases with the chemical formula $\text{C}_{2.1}\text{H}_{6.2}\text{O}_{2.16}$, a heat of combustion of $17,425\text{ kJ}\cdot\text{kg}^{-1}$, and a flame radiation fraction of 0.35, following Ref. [53]. Lagrangian particles are introduced 1 s after the start of the simulation to replicate the experimental procedure, in which branches were inserted into a fully developed hot flow. At the specified inlet gas velocity of $2.41\text{ m}\cdot\text{s}^{-1}$, consistent with the experimental conditions, this duration is sufficient to establish a stable flow field. A soot yield of 0.02 was specified in the combustion model, consistent with values commonly used in wildfire simulations [53, 60, 61]. CO production was neglected (CO yield set to zero) to simplify the chemistry, as the focus of this study is on ignition behavior rather than detailed species tracking. Previous studies have shown that soot, along with CO_2 and H_2O , dominates radiative heat transfer in the flaming combustion of fine vegetative fuels [62, 63], supporting this modeling choice.

The ignition process in the simulation is modeled using an external function designed to replicate the transition from glowing (smoldering) to flaming combustion observed in the experiments. This approach is illustrated in the flowchart in Fig. 12 and implemented using control logic functionality in FDS [59].

The process begins with the heating of the pine needle by external heat fluxes, primarily from the CIF. As the pine needle absorbs heat, its temperature gradually increases, leading to the release of pyrolysis gases. At each time step t , the maximum temperature of the pine needle particles is found. If this temperature exceeds a predefined critical solid temperature, $T_{s,cr}$, the ignition process is initiated, resulting in the ignition of the pyrolysis gases. To simplify the model, the autoignition temperature is set to 0 K at the computational cell corresponding to the measurement location (referred to as the “spark” location and illustrated in Fig. 11). In all other computational cells, the autoignition temperature remains at its pre-set value, 500 °C. This approach ensures that once the critical solid temperature threshold is reached at the spark location, gas-phase combustion becomes inevitable, signifying the rapid ignition of the fuel. In this simulation, gas-phase ignition is modeled via a simplified control logic, while char oxidation is omitted. The spark serves as a triggering mechanism for flaming ignition once the solid temperature threshold is reached, rather than an explicit model of the smoldering-to-flaming transition. This approach does not attempt to resolve the smoldering phase but instead uses a control-based ignition trigger to approximate the onset of flaming once sufficient heating of the solid has occurred. Although a char oxidation model is available in FDS [59], it was omitted in the present simulations to reduce model complexity. The study focuses on ignition thresholds and early flame propagation under wind-driven conditions, where flaming combustion of volatiles is the dominant mechanism and the role of char oxidation is limited.

Conversely, if the maximum temperature of the pine needle remains below $T_{s,cr}$, autoignition and gas-phase chemical reactions will not occur. While the pyrolysis gas from the vegetation primarily consists of methane [64], which has an autoignition temperature of 540 °C [65], the pre-set ignition temperature is intentionally lower. This adjustment compensates for the relatively coarse mesh size used in the simulation, which limits its ability to fully resolve the complexities of the gas-phase chemical reactions. Setting a lower autoignition temperature ensures that flame propagation in the gas-phase can be accurately modeled [59].

Another crucial parameter in the simulation is the initial unmixed fraction, ζ , evaluated at each time step. In the model, each computational cell is treated as a batch reactor, where only mixed compositions can react [59]. The evolution of ζ is governed by $d\zeta/dt = -\zeta/t_{mix}$, where t_{mix} represents the mixing time scale. This equation is influenced by the initial mixing conditions, which, by default, are fully non-premixed. In the experimental setup, the hot gases from the CIF mix with the pyrolysis gases released from the branches before ignition occurs. Since the computational cell size and the time step are sufficiently small, the mixing process can be effectively modeled. To simulate the initial mixing prior to ignition, the initial value of ζ is set to 0.9. Verification studies were conducted to evaluate the effects of varying the initial value of ζ . When $\zeta = 1$ (fully unmixed), under high fuel moisture content (FMC) conditions, ignition at the spark location is insufficient to generate

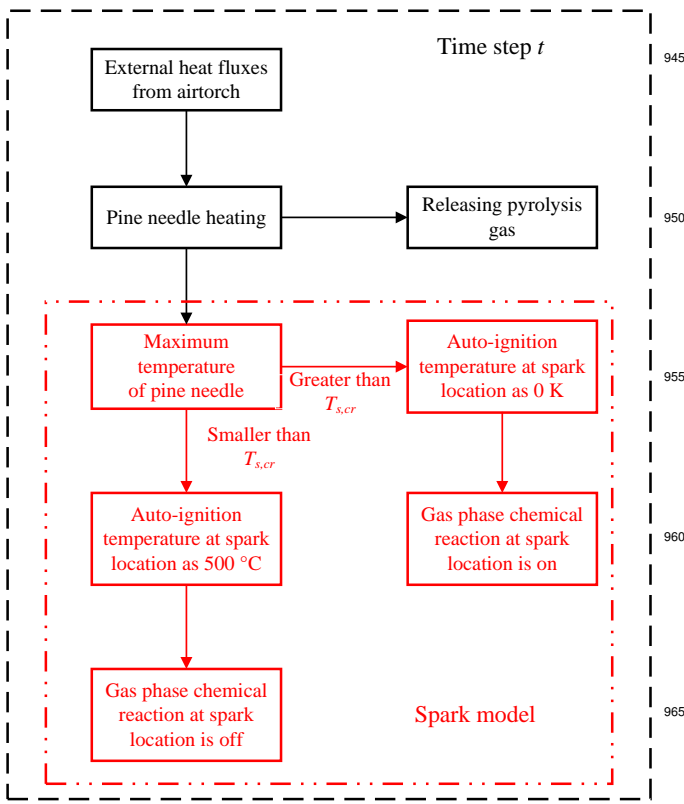


Figure 12: Flowchart depicting the ignition criteria implemented in the simulation, with the spark model highlighted in red.

enough heat to warm the surrounding cells, preventing flame propagation. Conversely, with $\zeta = 0.9$, the flame propagates from the ignition point to neighboring cells, triggering complete gas-phase ignition.

By establishing these clear temperature-based conditions (see Fig. 12), the simulation effectively replicates the real-world ignition dynamics observed in pine needles exposed to convective heating. Another parameter that must be defined beforehand is₉₈₀ the critical solid temperature, $T_{s,cr}$. The effects of this critical temperature are addressed in Section 4.2.

In simulations where air is the environmental gas, the activation energy, E_a , and pre-exponential factor, A , were selected based on thermogravimetric data for pine needles and bark in air, as shown in Figs. 10c and 10d. Since ignition occurs in an ambient environment with significant oxygen availability, using parameters that reflect air conditions ensures that the oxidation processes governing ignition and combustion are accurately represented. The presence of oxygen significantly influences the heterogeneous chemical kinetics, promoting exothermic reactions that drive ignition and subsequent fire spread [66]. Therefore, to model fire ignition realistically, it is crucial to adopt kinetic parameters that reflect the increased reactivity due to oxidative processes in the air. From the TGA analysis, the values of E_a and A were piecewise functions of the conversion degree with air as the environmental gas. The values were around $E_a \approx 45 - 55 \text{ kJ}\cdot\text{mol}^{-1}$ and $A \approx 10^4 - 10^7 \text{ s}^{-1}$ depending on the

material (i.e., needles vs. bark). In the simulation, E_a is chosen as 45 kJ·mol⁻¹ and A is chosen as 10⁵ s⁻¹ by averaging the pine needle and bark cases with the conversion degree ranging from 0.3 to 0.7 in an air environment. To account for the heterogeneous structure of the Douglas fir samples, pyrolysis kinetics were specified separately for the different components based on TGA data for pine needles and bark. Given their similar thermal decomposition behavior (cf. Fig. 10), these components were modeled using a unified set of kinetic parameters. The woody core of the branches, having slower decomposition and higher char yield, was assigned a distinct set of kinetic coefficients reflecting its lower volatility. Moisture evaporation was handled using the built-in single-step evaporation model in FDS, with initial moisture content specified for each component based on experimental measurements. This evaporation step occurs prior to pyrolysis, and assumes uniform moisture distribution within each component.

The ignition criteria used in the model ensures that the ignition mechanism shown in Fig. 12 and its associated thermal feedback are captured while maintaining computational efficiency. The model's accuracy hinges on capturing the critical threshold temperature that governs the transition between pyrolysis and autoignition, thus directly impacting the onset of gas-phase chemical reactions.

Figure 13 presents a comparison of the heat release rate per unit volume, HRRPUV, across three scenarios during the ignition process. The plenum of the CIF is shown at the bottom of the domain and the green rectangle represents the pine needles of the Douglas fir branch. The first panel (Fig. 13a) depicts the HRRPUV distribution without a spark model after 3 s when the hot gas comes into contact with the branch, which occurs faster than observed in the experiments. Hence, this result is inconsistent with experimental observations, as pyrolysis gases were released without ignition, and the heat released from subsequent combustion should ideally accelerate the pyrolysis process as heat feedback from the flame to the solid fuel is established. The overestimation of reaction initiation suggests that the initial model lacks proper control over the ignition phase. In contrast, the second and third panels (Figs. 13b and 13c) illustrate HRRPUV distributions at 14.9 s and 15 s, respectively, when the hot gases touch the branch, incorporating a localized ignition model. In these simulations, ignition is initiated at a specific location and then propagates outward through the domain. This localized ignition more accurately captures the experimental conditions, where flame spread occurs after a focused ignition point. The heat feedback from the flame to the pyrolysis process occurs later compared to the initial, non-localized model, which aligns more closely with experimental observations.

This delayed heat feedback and subsequent ignition propagation are further illustrated in Fig. 14. The figure compares the heat release rate, HRR, and mass loss rate, MLR, for two ignition models: one with a spark initiation model and one without. The HRR is shown on the left vertical axis in red, while the MLR is depicted on the right vertical axis in black. The re-

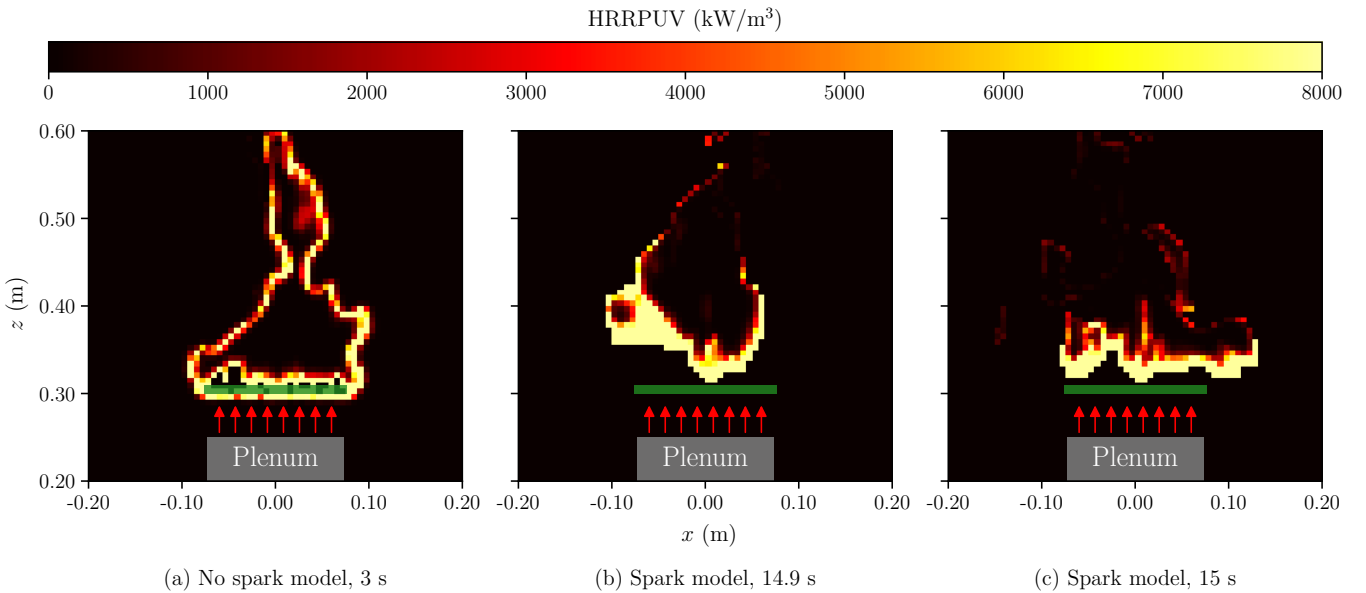


Figure 13: Heat release rate per unit volume (HRRPUV) near the sample (green rectangle) at various times after ignition. All cases correspond to a FMC of 5%, a critical solid temperature, $T_{s,cr}$, of 380 °C, and a gas temperature, T_{gas} , of 400 °C. Red arrows indicate the direction of hot gas flow exiting the CIF plenum. (a) Ignition without the spark model at 3 s; (b) ignition with the spark model at 14.9 s; (c) ignition with the spark model at 15 s.

sults highlight significant differences in both HRR and MLR depending on the inclusion of the spark model.

For the ignition without the spark model (dotted lines), the HRR reaches its peak very early in the process, indicating that combustion is initiated uniformly throughout the domain. This behavior leads to an overestimation of the combustion rate at the beginning, as evidenced by the sharp rise and subsequent rapid decline of HRR. The MLR follows a similar trend, peaking early and decreasing rapidly, which suggests that the pyrolysis process is prematurely accelerated in the absence of localized ignition control.

In contrast, the ignition with the spark model (solid lines) shows a more realistic progression of the combustion process. Here, the HRR begins to rise significantly only after the initial ignition event around 15 seconds, with the subsequent flame spread being more gradual. The HRR reaches a lower peak compared to the non-spark model but sustains for a longer period. This behavior aligns more closely with experimental observations, where ignition starts locally and propagates through the domain over time. The MLR with the spark model also demonstrates a smoother rise and fall. The decline of the first peak indicates that the branch is gradually undergoing pyrolysis, while the second peak reflects the heat received from the propagating gas flame and how the flame influences the branch's pyrolysis. These results indicate a more controlled pyrolysis process, consistent with the localized ignition that initiates pyrolysis in a more realistic sequence.

The comparison between the two models highlights the impact of incorporating a localized spark initiation model on capturing the ignition dynamics and heat release in the system. The spark ignition model provides a more gradual and sustained

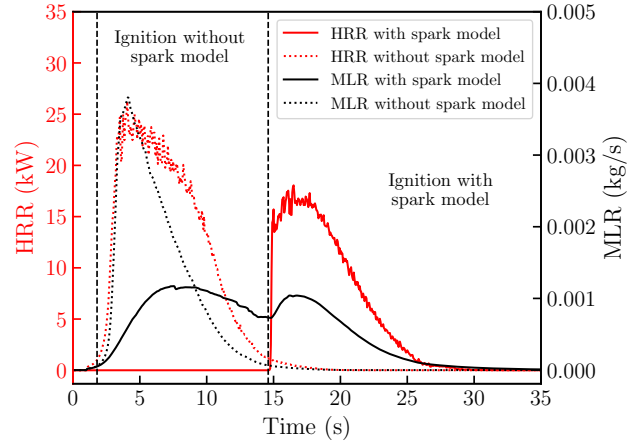


Figure 14: Comparison of heat release rate (HRR) and mass loss rate (MLR) from two different ignition methods, the current one proposed with the spark model and the model without spark model. Two vertical dashed lines show the ignition time with and without spark model

combustion process, better representing actual observed ignition behavior. In contrast, the non-spark model exaggerates the combustion rate due to the lack of localized initiation, resulting in unrealistic ignition and heat release patterns. This approach enables robust predictions of ignition behavior under varying conditions of external heat flux and needle temperature, ensuring the model captures the complex interplay of heat transfer, pyrolysis, and combustion inherent in wildfire scenarios. It provides a more realistic representation of the combustion dynamics.

In the experimental campaign, a subset of cases exhibited downstream ignition (see Section 3.1), where flaming ignition

occurred several centimeters above the fuel surface. In contrast, the simulations presented here, which employed a simplified ignition model based on solid temperature thresholds and localized spark triggering, consistently resulted in ignition near the sample region. The current model does not explicitly resolve ignition kernels forming far from the surface, as it is not designed to simulate detailed gas-phase mixing or chemical induction delays. Capturing such downstream ignition phenomena would require a refined treatment of gas-phase ignition chemistry and flow turbulence, which are beyond the scope of the present study but offer a promising direction for future modeling work.

4.2. Results from simulation

A key factor to examine in the simulation is the critical (threshold) solid temperature, $T_{s,cr}$, used to determine ignition. Figure 15 illustrates the ignition delay time as a function of gas temperature for various levels of fuel moisture content, FMC, ranging from 5% to 85%. The results highlight the significant influence of FMC on ignition behavior, with higher moisture content leading to longer ignition delay times due to the additional energy required to evaporate the moisture before ignition can occur.

As expected, the ignition threshold temperature plays a crucial role in determining whether ignition will occur and how long the ignition process takes. This temperature is closely related to the onset of the char oxidation process, where the heat generated from char oxidation drives the pyrolysis of surrounding vegetation. A portion of this heat is also lost to the environment through convection and radiation. Consequently, $T_{s,cr}$ represents the temperature at which the heat released by char oxidation will be sufficient not only to sustain pyrolysis but also to overcome the heat losses, thus leading to ignition. Additionally, $T_{s,cr}$ influences the ignition delay time. Higher values of $T_{s,cr}$ lead to longer ignition delay times, as more time is required for the system to accumulate sufficient energy to reach the ignition threshold. This effect is particularly evident at lower gas temperatures, where the ignition process is already hindered by a lack of thermal energy. Conversely, lower values of $T_{s,cr}$ facilitate quicker ignition, resulting in shorter ignition delay times across the entire range of gas temperatures. However, as the gas temperature increases, the influence of $T_{s,cr}$ on ignition delay diminishes, with delay times converging for different $T_{s,cr}$ values at higher temperatures.

The value of $T_{s,cr}$ directly affects the critical gas temperature required for ignition. For higher $T_{s,cr}$ values, the required gas temperature must also be higher to compensate for the increased energy threshold needed to achieve ignition. This relationship is evident in the shaded regions of each case in Fig. 15, which represent the conditions under which no ignition occurs. As $T_{s,cr}$ increases, the critical gas temperature for ignition rises accordingly, shifting the boundary between ignition and no-ignition conditions.

For the autoignition of wood, the ignition criterion is at low heating conditions is fundamentally related to the complex pro-

cess of char oxidation [30, 67]. For the sake of simplicity, in this work, as shown in the previous paragraph, ignition criteria is treated as a function of reaching a specific temperature threshold. However, it is important to recognize that a more comprehensive understanding of the ignition process requires further exploration, particularly focusing on the underlying chemical and thermal mechanisms.

One promising approach for understanding ignition mechanisms is the use of thermogravimetric analysis (TGA) in combination with differential scanning calorimetry (DSC), which provide insights into the thermal decomposition and oxidation processes of wood under various conditions. These techniques allow for a systematic examination of variables such as heating rates, ambient oxygen concentration, and wood composition on the onset of ignition. Instead of addressing these complexities, the approach taken in this study was to vary a single parameter to evaluate its effect on predicted ignition outcomes. While this simplification serves as a practical step for initial simulations, it may overlook important factors such as the kinetics of char formation and oxidation. Future studies incorporating experimental data from TGA and DSC will enable a more detailed investigation, refine ignition criteria, and improve the predictive capabilities of the model. Such research may provide scientific justification for the use of simplified approaches, like the one employed here, in simulations intended for engineering applications.

Figure 16 presents the heat release rate (HRR) as a function of time for different gas temperatures, T_{gas} , ranging from 400 °C to 500 °C. In this case, the FMC is set to 5%, and the critical solid temperature to 380 °C. Gas temperatures between 350 °C and 390 °C are excluded as no ignition was observed in this range. The color map, transitioning from blue to red, represents increasing gas temperatures, with each line corresponding to the HRR behavior at a specific temperature. As indicated by the color gradient, higher initial gas temperatures (e.g., 490–500 °C, represented by reddish lines) result in an earlier and more rapid rise in HRR. These cases exhibit a steep increase, reaching peak values of approximately 90–120 kW within the first few seconds, followed by a rapid decline. This trend suggests that elevated gas temperatures accelerate the ignition process, leading to a short but intense combustion phase.

Conversely, at lower initial gas temperatures (e.g., 400 °C, represented by blueish lines), the HRR peak occurs significantly later. The gradual rise in HRR suggests that ignition is delayed, requiring more time for the fuel to reach the necessary conditions for combustion. Additionally, the peak HRR values for these lower-temperature cases are comparatively lower, indicating a less intense combustion process. The overall trend, as highlighted by the arrow, confirms that as the initial gas temperature increases, the ignition time decreases, and the combustion intensity rises sharply.

Figure 17 presents the heat release rate, HRR, over time for different levels of fuel moisture content, FMC, ranging from 5% to 85%, reflecting values observed in the experiments, at gas temperatures of 450 °C, and a solid critical temperature of

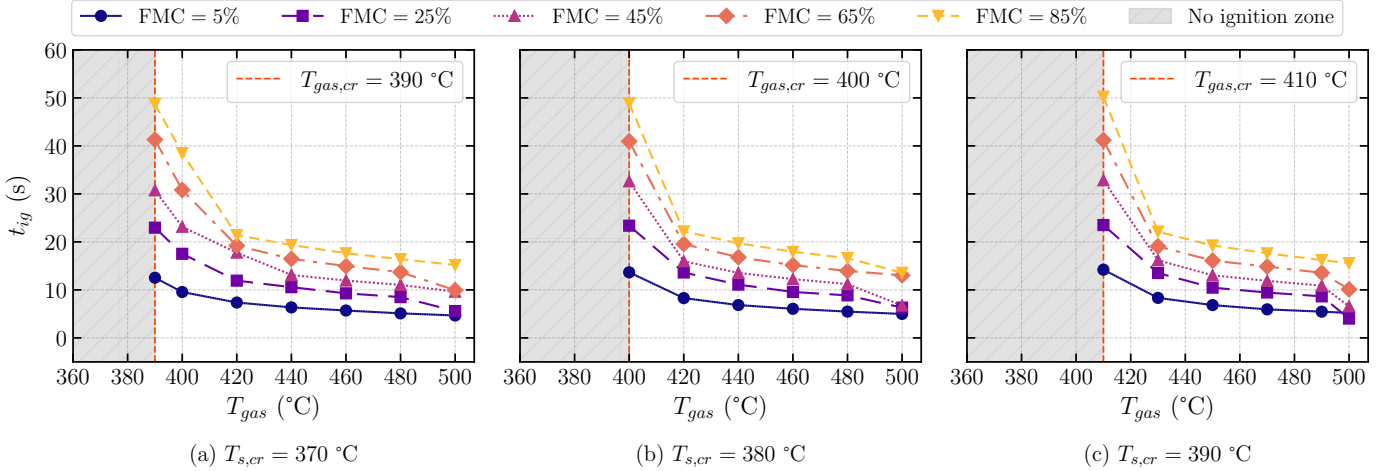


Figure 15: Simulation results for the ignition delay times vs. gas temperature at different critical solid temperature thresholds for ignition, $T_{s,cr}$, and fuel moisture contents (FMC). (a) $T_{s,cr} = 370^{\circ}\text{C}$, (b) $T_{s,cr} = 380^{\circ}\text{C}$, and (c) $T_{s,cr} = 390^{\circ}\text{C}$

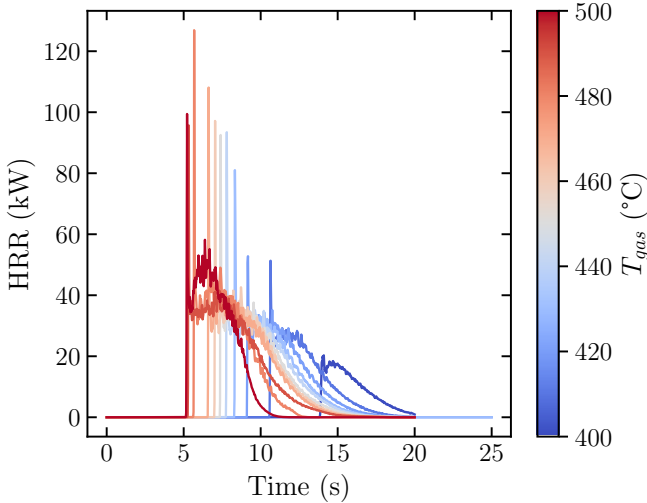


Figure 16: Heat release rate for different gas temperature of pine branch ignition with FMC = 5% and $T_{s,cr} = 380^{\circ}\text{C}$.

380 °C. The figure illustrates the impact of increasing FMC on the ignition process and combustion characteristics. The colormap from yellow to purple represents increasing FMC, with dark purple corresponding to 85% and yellow to 5%. The figure clearly shows that FMC influences ignition behavior and combustion dynamics. As FMC increases, the ignition delay time also increases. For instance, at 5% FMC, ignition occurs rapidly with a sharp HRR peak around 7.5 seconds. However, as FMC increases to 85%, the HRR peak shifts to later times, occurring closer to 24 seconds, indicating a substantial delay in the ignition process. This trend shows that higher FMC leads to prolonged ignition times in the simulations due to the increased energy required to evaporate the moisture content before ignition can occur.

Furthermore, the peak HRR is also influenced by FMC, with lower FMC resulting in a higher HRR peak. At 5% FMC, the

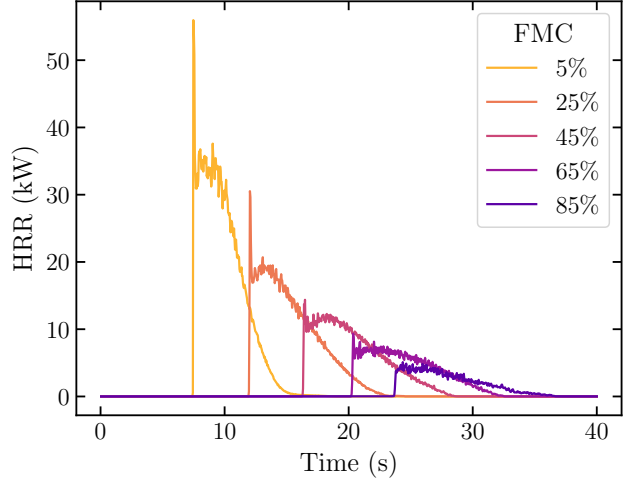


Figure 17: Simulated heat release rate (HRR) as a function of time for various fuel moisture content (FMC) cases at a gas temperature of $T_{gas} = 450^{\circ}\text{C}$, with a critical solid temperature of $T_{s,cr} = 380^{\circ}\text{C}$.

HRR peaks at approximately 55 kW, while at 85% FMC, the HRR peak is significantly lower, around 5 kW. This reduction in peak HRR can be attributed to the increased FMC, which not only delays ignition but also absorbs a considerable amount of energy, thereby reducing the heat available for combustion. The higher gas temperature provides more thermal energy to overcome the FMC, resulting in faster ignition.

Although HRR is not directly validated against experimental data in this study, it is included here as a diagnostic quantity to aid interpretation of model behavior. These visualizations provide insight into the spatial development and propagation of ignition in response to different modeling assumptions (e.g., with or without a spark model).

Figure 18 presents ignition delay times for various gas temperatures and fuel moisture content (FMC) levels, comparing sim-

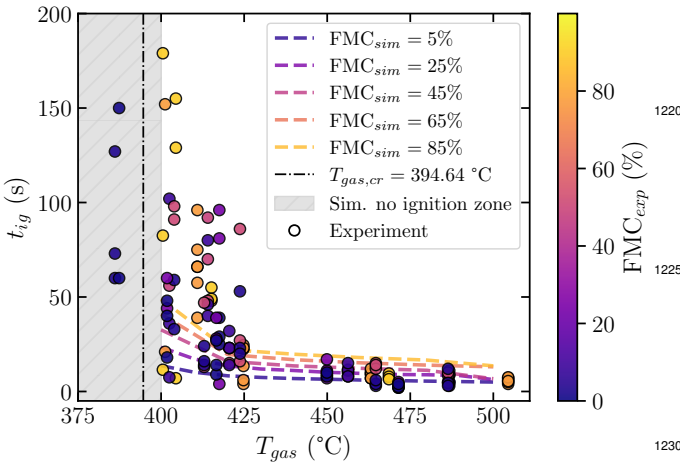


Figure 18: Experimental (markers) and simulated (lines) ignition delay time at different gas temperatures. The colors represent the fuel moisture content (FMC). For the simulated data, the critical solid temperature for ignition was set to $T_{s,cr} = 380^\circ\text{C}$.

ulation results (FMC_{sim} ; dashed lines) with experimental data (FMC_{exp} ; circle markers). The FMC_{sim} ranges from 5% to 85%, represented by different line colors (shown in the legend), while the experimental data also cover a similar range of FMC¹²⁴⁰ values, represented in the color palette. The shaded area represent the region where no ignition occurs in the simulation (with $T_{s,cr} = 380^\circ\text{C}$, cf. Fig. 15b). The comparison highlights that for lower FMC levels (e.g., 5% and 25%), the ignition delay times from the simulation closely align with the experimental results, suggesting that the model effectively captures the ignition dynamics under low-moisture conditions where the pyrolysis process is less hindered. However, as FMC increases to higher levels (e.g., 65% and 85%), the discrepancies between the simulation and experimental ignition delay times become more apparent. Specifically, the simulations tend to underestimate the ignition delay time compared to the experimental¹²⁵⁰ data at higher moisture levels. This difference suggests that the model may not fully account for the complexities associated with moisture evaporation and its interaction with heat transfer and/or gas-phase combustion kinetics leading to faster predicted ignition than observed experimentally. The presence of moisture significantly affects the rate of char oxidation, the pyrolysis process, and the heat transfer dynamics, which are challenging to accurately capture in a simulation [68]. While the relationship between increasing FMC and longer ignition delay times is not visually apparent in Fig. 18, this trend was previously demonstrated through statistical analysis of the experimental data (cf. Section 3.1). Specifically, for $T_{gas} \leq 440^\circ\text{C}$, ignition delay times exhibited greater variability at higher FMC and more consistency at lower FMC. A t-test comparing high and low FMC groups, with a median FMC of 23%, yielded a statistically significant difference ($p = 0.024$), indicating that FMC does influence ignition delay under these conditions.

Another key observation is related to the critical gas temperature for ignition, denoted as $T_{gas,cr}$ in Fig. 18 (dashed vertical

black line). In the experiments, it was found that a single critical gas temperature predicted the ignition outcome well overall, but the agreement was less good for dry fuels (low FMC), as shown in Fig. 4. At low FMC values (<10%), this critical gas temperature is roughly 380°C , lower than the overall value from the experiments. At FMC values (>10%) the critical gas temperature changes less with FMC. On the other hand, the model does not capture this effect indicating that FMC may influence flammability in a way not considered in this model.

Overall, the simulation successfully captures the general trend of increasing ignition delay time with increasing FMC and decreasing gas temperature. However, the discrepancies observed at lower FMC levels or low gas temperatures highlighting areas where the model could be refined to improve accuracy, particularly in modeling the heat required to evaporate moisture and the thermal feedback between char oxidation and pyrolysis. Additionally, the experimental data provide valuable insight into real-world ignition conditions, emphasizing the importance of accounting for variability in vegetation characteristics and environmental factors, such as convection and heterogeneity. Meanwhile, as the system approaches critical ignition conditions, gas-phase reactions between volatile gases and oxygen become increasingly significant. The exothermicity of these reactions can amplify local temperatures, creating a positive feedback loop that accelerates ignition, which is successfully captured in the simulation.

5. Conclusions

The convective ignition experiments revealed that fuel moisture content (FMC) influences ignition dynamics. Lower FMC resulted reduced critical gas temperatures ($T_{gas,cr}$) required for ignition. Logistic regression confirmed the dependence of $T_{gas,cr}$ on FMC. High-speed imaging captured gas-phase ignition in 25 cases, where flame propagation and flame height increased with decreasing FMC, reflecting enhanced energy release from faster combustion rates. The transition from glowing combustion to flaming ignition, characterized by Δt , was consistently observed, highlighting glowing combustion as a precursor to flaming autoignition under various conditions.

Thermogravimetric analysis (TGA) complemented these findings by providing thermal decomposition data, differentiating the behaviors of bark and pine needles, and yielding kinetic parameters essential for simulation accuracy. These parameters were incorporated into the Fire Dynamics Simulator (FDS) to model ignition behavior, pyrolysis, and gas-phase interactions. A heat transfer model applied to a cylindrical element successfully predicted ignition delay times at higher gas temperatures, where ignition delay times approximated pyrolysis times. However, near critical thresholds, the model's accuracy decreased due to the dominant and complex role of gas-phase reactions.

Numerical simulations using FDS captured key ignition dynamics, including flame propagation and the effects of FMC on thermal decomposition and heat transfer. Enhanced simulation protocols allowed for detailed modeling of gas-phase

ignition, aligning well with experimental observations. These combined experimental and simulation results underscore the critical roles of FMC, gas temperature, and heat transfer in controlling biomass ignition. The findings contribute to a nuanced understanding of ignition processes and provide insights into biomass combustion behavior under real-world conditions.

6. Supplementary material

Supplementary material, including example FDS input files and additional resources, is publicly available at: https://github.com/javaldivia/conductive_ignition.

7. Acknowledgments

Funding for this project was provided by the California Department of Forestry and Fire Protection's Forest Health Program as part of the California Climate Investments Program (Grant No. 8GG21827). The authors sincerely thank Frederick Brokaw, Laboratory Director at WPI, for his invaluable assistance and expertise in facilitating the experiments. The authors also acknowledge the endowed Pearsall Fund at WPI for supporting the acquisition of the high-speed camera used in this study.

8. Bibliography

- [1] A. Simeoni, Wildland fires, in: M. J. Hurley (Ed.), SFPE handbook of fire protection engineering, 5th Edition, Springer, 2016, pp. 3283–3302. [doi:10.1007/978-1-4939-2565-0_87](https://doi.org/10.1007/978-1-4939-2565-0_87).
- [2] F. A. Williams, Urban and wildland fire phenomenology, *Progress in Energy and Combustion Science* 8 (4) (1982) 317–354. [doi:10.1016/0360-1285\(82\)90004-1](https://doi.org/10.1016/0360-1285(82)90004-1).
- [3] A. D. Syphard, T. J. Brennan, J. E. Keeley, The role of defensible space for residential structure protection during wildfires, *International Journal of Wildland Fire* 23 (8) (2014) 1165–1175. [doi:10.1071/WF13158](https://doi.org/10.1071/WF13158).
- [4] G. Winter, S. McCaffrey, C. A. Vogt, The role of community policies in defensible space compliance, *Forest Policy and Economics* 11 (8) (2009) 570–578. [doi:10.1016/j.forepol.2009.07.004](https://doi.org/10.1016/j.forepol.2009.07.004).
- [5] M. Yebra, P. E. Dennison, E. Chuvieco, D. Riaño, P. Zylstra, E. R. Hunt, F. M. Danson, Y. Qi, S. Jurdao, A global review of remote sensing of live fuel moisture content for fire danger assessment: Moving towards operational products, *Remote Sensing of Environment* 136 (2013) 455–468. [doi:10.1016/j.rse.2013.05.029](https://doi.org/10.1016/j.rse.2013.05.029).
- [6] R. E. Burgan, Estimating live fuel moisture for the 1978 National Fire Danger Rating System, Tech. Rep. INT-226, USDA Forest Service, Intermountain forest and range experiment station, Ogden, Utah 84401 (1979). [doi:10.5962/bhl.title.68713](https://doi.org/10.5962/bhl.title.68713).
- [7] R. M. Nelson, Chapter 4 - water relations of forest fuels, in: E. A. Johnson, K. Miyanishi (Eds.), *Forest Fires*, Academic Press, San Diego, 2001, pp. 79–149. [doi:https://doi.org/10.1016/B978-012386660-8/50006-4](https://doi.org/10.1016/B978-012386660-8/50006-4).
- [8] D. X. Viegas, M. Viegas, A. Ferreira, Moisture content of fine forest fuels and fire occurrence in central portugal, *International Journal of Wildland Fire* 2 (2) (1992) 69–86. [doi:10.1071/WF9920069](https://doi.org/10.1071/WF9920069).
- [9] R. H. White, D. R. Weise, K. Mackes, A. C. Dibble, Cone calorimeter testing of vegetation: an update, in: Proceedings of the 35th international conference on fire safety, Products Safety Corporation Sissonville, West Virginia, USA, 2002, pp. 22–24.
- [10] M. G. Etlinger, F. C. Beall, Development of a laboratory protocol for fire performance of landscape plants, *International Journal of Wildland Fire* 13 (4) (2004) 479–488. [doi:10.1071/WF04039](https://doi.org/10.1071/WF04039).
- [11] D. R. Weise, R. H. White, F. C. Beall, M. Etlinger, Use of the cone calorimeter to detect seasonal differences in selected combustion characteristics of ornamental vegetation, *International Journal of Wildland Fire* 14 (3) (2005) 321–338. [doi:10.1071/WF04035](https://doi.org/10.1071/WF04035).
- [12] A. C. Dibble, R. H. White, P. K. Lebow, Combustion characteristics of north-eastern USA vegetation tested in the cone calorimeter: invasive versus non-invasive plants, *International Journal of Wildland Fire* 16 (4) (2007) 426–443. [doi:10.1071/WF05103](https://doi.org/10.1071/WF05103).
- [13] A. Simeoni, *Experimental Understanding of Wildland Fires*, John Wiley & Sons, Ltd, 2013, Ch. 3, pp. 35–52. [doi:https://doi.org/10.1002/9781118529539.ch3](https://doi.org/10.1002/9781118529539.ch3).
- [14] J. C. Thomas, A. Simeoni, M. Gallagher, N. Skowronski, An experimental study evaluating the burning dynamics of pitch pine needle beds using the FPA, *Fire Safety Science* 11 (2014) 1406–1419. [doi:10.3801/IAFSS.FSS.11-1406](https://doi.org/10.3801/IAFSS.FSS.11-1406).
- [15] M. El Houssami, J. C. Thomas, A. Lamorlette, D. Morvan, M. Chaos, R. Hadden, A. Simeoni, Experimental and numerical studies characterizing the burning dynamics of wildland fuels, *Combustion and Flame* 168 (2016) 113–126. [doi:10.1016/j.combustflame.2016.04.004](https://doi.org/10.1016/j.combustflame.2016.04.004).
- [16] M. J. Spearpoint, J. G. Quintiere, Predicting the piloted ignition of wood in the cone calorimeter using an integral model—effect of species, grain orientation and heat flux, *Fire Safety Journal* 36 (4) (2001) 391–415. [doi:10.1016/S0379-7112\(00\)00055-2](https://doi.org/10.1016/S0379-7112(00)00055-2).
- [17] P. Mindykowski, A. Fuentes, J. Consalvi, B. Porterie, Piloted ignition of wildland fuels, *Fire Safety Journal* 46 (1-2) (2011) 34–40. [doi:10.1016/j.firesaf.2010.09.003](https://doi.org/10.1016/j.firesaf.2010.09.003).
- [18] J. Rivera, N. Hernández, J. Consalvi, P. Reszka, J. Contreras, A. Fuentes, Ignition of wildland fuels by idealized firebrands, *Fire Safety Journal* 120 (2021) 103036. [doi:10.1016/j.firesaf.2020.103036](https://doi.org/10.1016/j.firesaf.2020.103036).
- [19] A. L. Sullivan, Inside the inferno: Fundamental processes of wildland fire behaviour: Part 2: Heat transfer and interactions, *Current Forestry Reports* 3 (2017) 150–171. [doi:10.1007/s40725-017-0058-z](https://doi.org/10.1007/s40725-017-0058-z).
- [20] K. M. Yedinak, J. D. Cohen, J. M. Forthofer, M. A. Finney, An examination of flame shape related to convection heat transfer in deep-fuel beds, *International Journal of Wildland Fire* 19 (2) (2010) 171–178. [doi:10.1071/WF07143](https://doi.org/10.1071/WF07143).
- [21] T. Beer, The interaction of wind and fire, *Boundary-Layer Meteorology* 54 (3) (1991) 287–308. [doi:10.1007/BF00183958](https://doi.org/10.1007/BF00183958).
- [22] X. Zhou, S. Mahalingam, D. Weise, Modeling of marginal burning state of fire spread in live chaparral shrub fuel bed, *Combustion and Flame* 143 (3) (2005) 183–198. [doi:10.1016/j.combustflame.2005.05.013](https://doi.org/10.1016/j.combustflame.2005.05.013).
- [23] A. C. Fernandez-Pello, The solid phase, in: G. Cox (Ed.), *Combustion Fundamentals of Fire*, Academic Press, 1994, Ch. 2, pp. 31–100.
- [24] T. Niioka, M. Takahashi, M. Izumikawa, Gas-phase ignition of a solid fuel in a hot stagnation-point flow, in: *Symposium (International) on Combustion*, Vol. 18, Elsevier, 1981, pp. 741–747. [doi:10.1016/S0082-0784\(81\)80078-1](https://doi.org/10.1016/S0082-0784(81)80078-1).
- [25] N. Roenner, G. Rein, Convective ignition of polymers: New apparatus and application to a thermoplastic polymer, *Proceedings of the Combustion Institute* 37 (2019) 4193–4200. [doi:10.1016/j.proci.2018.05.180](https://doi.org/10.1016/j.proci.2018.05.180).
- [26] S. McAllister, M. Finney, Autoignition of wood under combined convective and radiative heating, *Proceedings of the Combustion Institute* 36 (2017) 3073–3080. [doi:10.1016/j.proci.2016.06.110](https://doi.org/10.1016/j.proci.2016.06.110).
- [27] S. McAllister, M. Finney, Convection ignition of live forest fuels, *Fire Safety Science* 11 (2014) 1312–1325. [doi:10.3801/IAFSS.FSS.11-1312](https://doi.org/10.3801/IAFSS.FSS.11-1312).
- [28] A. M. Phillips, H. A. Becker, Pyrolysis and burning of single sticks of pine in a uniform field of temperature, gas composition, and gas velocity, *Combustion and Flame* 46 (1982) 221–251. [doi:10.1016/0010-2180\(82\)90019-0](https://doi.org/10.1016/0010-2180(82)90019-0).
- [29] R. A. Schroeder, Post-fire analysis of construction materials, Ph.D. thesis, University of California, Berkeley (1999).
- [30] N. Boonmee, J. G. Quintiere, Glowing and flaming autoignition of wood, *Proceedings of the Combustion Institute* 29 (1) (2002) 289–296. [doi:10.1016/S1540-7489\(02\)80039-6](https://doi.org/10.1016/S1540-7489(02)80039-6).
- [31] N. Boonmee, J. G. Quintiere, A theoretical investigation of surface glowing ignition leading to gas flaming autoignition, *Fire Safety Science* 8 (2005) 139–150. [doi:10.3801/IAFSS.FSS.8-139](https://doi.org/10.3801/IAFSS.FSS.8-139).
- [32] C. Anand, B. Shotorban, S. Mahalingam, S. McAllister, D. R. Weise, Physics-based modeling of live wildland fuel ignition experiments in the forced ignition and flame spread test apparatus, *Combustion Science and Technology* 189 (9) (2017) 1551–1570. [doi:10.1080/00102202.2017.1308357](https://doi.org/10.1080/00102202.2017.1308357).

- 1400 [33] E. Mueller, W. Mell, A. Simeoni, Large eddy simulation of forest canopy flow for wildland fire modeling, *Canadian Journal of Forest Research* 44 (12) (2014) 1534–1544. [doi:10.1139/cjfr-2014-0184](https://doi.org/10.1139/cjfr-2014-0184).
- 1405 [34] M. Vanella, K. McGrattan, R. McDermott, G. Forney, W. Mell, E. Gissi, P. Fiorucci, A multi-fidelity framework for wildland fire behavior simulations over complex terrain, *Atmosphere* 12 (2) (2021) 273. [doi:10.3390/atmos12020273](https://doi.org/10.3390/atmos12020273).
- 1410 [35] X. Ren, D. Zeng, Y. Wang, G. Xiong, G. Agarwal, M. Gollner, Temperature measurement of a turbulent buoyant ethylene diffusion flame using a dual-thermocouple technique, *Fire Safety Journal* 120 (2021) 103061. [doi:10.1016/j.firesaf.2020.103061](https://doi.org/10.1016/j.firesaf.2020.103061).
- 1415 [36] G. Di Cristina, R. A. Bryant, Comparison of two flow measurement devices for use in fire experiments, *Proceedings of the Combustion Institute* 40 (1-4) (2024) 105557. [doi:10.1016/j.proci.2024.105557](https://doi.org/10.1016/j.proci.2024.105557).
- 1420 [37] A. Singh, R. M. Ziazi, A. Simeoni, Intermittent fireline behaviour over porous vegetative media in different crossflow conditions, *International Journal of Wildland Fire* (2023). [doi:10.1071/WF22153](https://doi.org/10.1071/WF22153).
- 1425 [38] N. Boonmee, J. Quintiere, Glowing ignition of wood: the onset of surface combustion, *Proceedings of the Combustion Institute* 30 (2) (2005) 2303–2310. [doi:https://doi.org/10.1016/j.proci.2004.07.022](https://doi.org/10.1016/j.proci.2004.07.022).
- 1430 [39] L. G. Fraga, J. Silva, S. Teixeira, D. Soares, M. Ferreira, J. Teixeira, Influence of operating conditions on the thermal behavior and kinetics of pine wood particles using thermogravimetric analysis, *Energies* 13 (11) (2020) 2756. [doi:10.3390/en13112756](https://doi.org/10.3390/en13112756).
- 1435 [40] J. L. Urban, C. D. Zak, J. Song, C. Fernandez-Pello, Smoldering spot ignition of natural fuels by a hot metal particle, *Proceedings of the Combustion Institute* 36 (2017) 3211–3218. [doi:10.1016/j.proci.2016.09.014](https://doi.org/10.1016/j.proci.2016.09.014).
- 1440 [41] J. L. Urban, J. Song, S. Santamaría, C. Fernandez-pello, Ignition of a spot smolder in a moist fuel bed by a firebrand, *Fire Safety Journal* 108 (2019) 102833. [doi:10.1016/j.firesaf.2019.102833](https://doi.org/10.1016/j.firesaf.2019.102833).
- 1445 [42] A. Simeoni, J. C. Thomas, P. Bartoli, P. Borowiecki, P. Reszka, F. Colella, P. A. Santoni, J. L. Torero, Flammability studies for wildland and wildland-urban interface fires applied to pine needles and solid polymers, *Fire Safety Journal* 54 (2012) 203–217. [doi:10.1016/j.firesaf.2012.08.005](https://doi.org/10.1016/j.firesaf.2012.08.005).
- 1450 [43] T. Fateh, F. Richard, B. Batiot, T. Rogaume, J. Luche, J. Zaida, Characterization of the burning behavior and gaseous emissions of pine needles in a cone calorimeter - ftir apparatus, *Fire Safety Journal* 82 (2016) 91–100. [doi:10.1016/j.firesaf.2016.03.008](https://doi.org/10.1016/j.firesaf.2016.03.008).
- 1455 [44] S. McAllister, I. Grenfell, A. Hadlow, W. M. Jolly, M. Finney, J. Cohen, Piloted ignition of live forest fuels, *Fire Safety Journal* 51 (2012) 133–142. [doi:10.1016/j.firesaf.2012.04.001](https://doi.org/10.1016/j.firesaf.2012.04.001).
- 1460 [45] P. Reszka, J. Cruz, J. Valdivia, F. González, J. Rivera, C. Carvajal, A. Fuentes, Ignition delay times of live and dead *pinus radiata* needles, *Fire Safety Journal* 112 (2020) 102948. [doi:10.1016/j.firesaf.2020.102948](https://doi.org/10.1016/j.firesaf.2020.102948).
- 1465 [46] J. Torero, Flaming ignition of solid fuels, in: M. J. Hurley (Ed.), *SFPE Handbook of Fire Protection Engineering*, 5th Edition, Springer New York, New York, 2016, pp. 633–661. [doi:10.1007/978-1-4939-2565-0_21](https://doi.org/10.1007/978-1-4939-2565-0_21).
- 1470 [47] S. Martin, Diffusion-controlled ignition of cellulosic materials by intense radiant energy, *Symposium (International) on Combustion* 10 (1) (1965) 877–896, tenth Symposium (International) on Combustion. [doi:10.1016/S0082-0784\(65\)80232-6](https://doi.org/10.1016/S0082-0784(65)80232-6).
- 1475 [48] S. Whitaker, Forced convection heat transfer correlations for flow in pipes, past flat plates, single cylinders, single spheres, and for flow in packed beds and tube bundles, *AICHe Journal* 18 (2) (1972) 361–371. [doi:10.1002/aic.690180219](https://doi.org/10.1002/aic.690180219).
- 1480 [49] J. R. Howell, M. P. Mengüç, K. Daun, R. Siegel, Thermal radiation heat transfer, 7th Edition, CRC press, 2021.
- 1485 [50] J. R. Howell, A catalog of radiation configuration factors, 3rd Edition, McGraw-Hill, 1982.
- 1490 [51] M. Modest, View factors, in: *Radiative Heat Transfer*, 4th Edition, Academic Press, 2022, Ch. 4. [doi:10.1016/B978-0-12-818143-0-00012-2](https://doi.org/10.1016/B978-0-12-818143-0-00012-2).
- 1495 [52] H. Sadiq, M. Wong, J. Tashan, R. Al-Mahaidi, X.-L. Zhao, Determination of steel emissivity for the temperature prediction of structural steel members in fire, *Journal of Materials in Civil Engineering* 25 (2) (2013) 167–173. [doi:10.1061/\(ASCE\)MT.1943-5533.0000607](https://doi.org/10.1061/(ASCE)MT.1943-5533.0000607).
- 1500 [53] W. Mell, A. Maranghides, R. McDermott, S. L. Manzello, Numerical simulation and experiments of burning Douglas fir trees, *Combustion and Flame* 156 (10) (2009) 2023–2041. [doi:10.1016/j.combustflame.2009.06.015](https://doi.org/10.1016/j.combustflame.2009.06.015).
- [54] J. C. Butcher, *Numerical methods for ordinary differential equations*, John Wiley & Sons, 2016. [doi:10.1002/9781119121534](https://doi.org/10.1002/9781119121534).
- [55] K. Slopiecka, P. Bartocci, F. Fantozzi, Thermogravimetric analysis and kinetic study of poplar wood pyrolysis, *Applied Energy* 97 (2012) 491–497. [doi:10.1016/j.apenergy.2011.12.056](https://doi.org/10.1016/j.apenergy.2011.12.056).
- [56] M. G. Grønli, G. Várhegyi, C. Di Blasi, Thermogravimetric analysis and devolatilization kinetics of wood, *Industrial & Engineering Chemistry Research* 41 (17) (2002) 4201–4208. [doi:10.1021/ie0201157](https://doi.org/10.1021/ie0201157).
- [57] A. Anca-Couce, N. Zobel, A. Berger, F. Behrendt, Smouldering of pine wood: Kinetics and reaction heats, *Combustion and Flame* 159 (4) (2012) 1708–1719. [doi:10.1016/j.combustflame.2011.11.015](https://doi.org/10.1016/j.combustflame.2011.11.015).
- [58] M. Poletto, Lignin: Trends and Applications, IntechOpen, 2018. [doi:10.5772/intechopen.68464](https://doi.org/10.5772/intechopen.68464).
- [59] K. McGrattan, S. Hostikka, R. McDermott, J. Floyd, C. Weinschenk, K. Overholt, Fire dynamics simulator user's guide, NIST special publication 1019 (6) (2013) 1–339. [doi:10.6028/NIST.SP.1019](https://doi.org/10.6028/NIST.SP.1019).
- [60] M. M. Valero, L. Jofre, R. Torres, Multifidelity prediction in wildfire spread simulation: Modeling, uncertainty quantification and sensitivity analysis, *Environmental Modelling & Software* 141 (2021) 105050. [doi:10.1016/j.envsoft.2021.105050](https://doi.org/10.1016/j.envsoft.2021.105050).
- [61] E. V. Mueller, Z. Campbell-Lochrie, C. Walker-Ravena, R. M. Hadden, Numerical simulations of flame spread in pine needle beds using simple thermal decomposition models, *Fire Safety Journal* 141 (2023) 103886. [doi:https://doi.org/10.1016/j.firesaf.2023.103886](https://doi.org/10.1016/j.firesaf.2023.103886).
- [62] A. T. Modak, Radiation from products of combustion, *Fire Safety Journal* 1 (6) (1979) 339–361. [doi:https://doi.org/10.1016/0379-7112\(79\)90004-3](https://doi.org/10.1016/0379-7112(79)90004-3).
- [63] W. Węgrzyński, G. Vigne, Experimental and numerical evaluation of the influence of the soot yield on the visibility in smoke in cfd analysis, *Fire Safety Journal* 91 (2017) 389–398. [doi:10.1016/j.firesaf.2017.03.053](https://doi.org/10.1016/j.firesaf.2017.03.053).
- [64] W. Gong, J. Cuevas, P. Reszka, A. Simeoni, The role of smoldering in the ignition of *pinus palustris* needles, *Fire Safety Journal* 143 (2024) 104053. [doi:10.1016/j.firesaf.2023.104053](https://doi.org/10.1016/j.firesaf.2023.104053).
- [65] M. G. Zabetakis, Flammability characteristics of combustible gases and vapors, *Tech. Rep. BM-BULL-627*, 7328370 (May 1964). [doi:10.2172/7328370](https://doi.org/10.2172/7328370).
- [66] A. N. Howell, E. L. Belmont, S. S. McAllister, M. A. Finney, An investigation of oxygen availability in spreading fires, *Fire Technology* 59 (4) (2023) 2147–2176. [doi:10.1007/s10694-023-01396-6](https://doi.org/10.1007/s10694-023-01396-6).
- [67] M. Gee, Modeling solid phase kinetics for burning live vegetation fuels, Master's thesis, Oregon State University (2024).
- [68] F. G. Fonseca, A. Funke, A. Niebel, A. P. Soares Dias, N. Dahmen, Moisture content as a design and operational parameter for fast pyrolysis, *Journal of Analytical and Applied Pyrolysis* 139 (2019) 73–86. [doi:10.1016/j.jaap.2019.01.012](https://doi.org/10.1016/j.jaap.2019.01.012).
- [69] J. R. Taylor, *An introduction to error analysis: the study of uncertainties in physical measurements*, 2nd Edition, University Science Books, 1997.
- [70] J. Y. Yeo, B. L. F. Chin, J. K. Tan, Y. S. Loh, Comparative studies on the pyrolysis of cellulose, hemicellulose, and lignin based on combined kinetics, *Journal of the Energy Institute* 92 (1) (2019) 27–37. [doi:10.1016/j.joei.2017.12.003](https://doi.org/10.1016/j.joei.2017.12.003).

Appendix A. Hot-flow mapping and uncertainty

Velocity and gas temperature fields above the plenum outlet were mapped using a three-dimensional traverse system (Iisel Germany LES5-L1290 with controller C142-4) combined with a data acquisition system implemented in Python via Arduino, as shown in Fig. A.19. Measurements were obtained with an S-type Pitot tube and a 36 AWG thermocouple at three vertical planes ($z = 19, 44.5$, and 88.9 mm), with the last plane corresponding to the vertical center of the sample location (cf. Fig. 1b, $z = 3.5$ in).



Figure A.19: Isel Germany 3D traverse system and the Convective Ignition Facility (CIF).

The analysis presented here corresponds to a mass flow rate of $500 \text{ s} \cdot \text{L} \cdot \text{min}^{-1}$ set at the mass flow controller and a gas temperature of 650°C set at the airtorch PID controller (measured inside the airtorch). Under these settings, conditions at the sample center were measured as $T_{\text{gas}} \approx 415^\circ\text{C}$ and $v_{\text{gas}} \approx 2.41 \text{ m} \cdot \text{s}^{-1}$. Flow data at each spatial point were recorded for 45 s at a sampling rate of 4 Hz, with a spatial resolution of 21.67 mm in both x and y directions, covering and extending beyond the plenum outlet. The measured velocity fields and associated experimental uncertainties are presented in Figs. A.20 and A.21, respectively.

Figures A.20 and A.22 present the interpolated velocity and temperature fields at the three measurement planes ($z = 19$, 44.5, and 88.9 mm). Velocity values were derived from the differential pressure Δp using the relation provided in Eq. (1).

Uncertainty in the mean velocity was estimated by combining the statistical error (standard error of the mean) with the propagated uncertainties in pressure and temperature, following standard methods [69]:

$$\delta_{\bar{v}_{\text{gas}}} = \sqrt{\left(\frac{\sigma_{v_{\text{gas}}}}{\sqrt{N}}\right)^2 + \left[\left(\frac{\partial v_{\text{gas}}}{\partial \Delta p} \cdot \delta_{\Delta p}\right)^2 + \left(\frac{\partial v_{\text{gas}}}{\partial T} \cdot \delta_T\right)^2\right]}, \quad (\text{A.1})$$

where $\delta_{\Delta p}$ includes both the standard deviation of Δp and the 3% reading error of the Sensirion SDP810-125 transducer, and δ_T corresponds to the observed variability in thermocouple readings. Systematic uncertainty was found to be dominated by the pressure component, contributing over 96% across all planes.

Temperature fields exhibit a gradual vertical decay, with average values of 403.3, 366.7, and 319.4°C at $z = 19$, 44.5, and 88.9 mm, respectively. Though gradients are present, the vertical variation remains within the same order of magnitude as the measurement uncertainty (typically 70 – 85°C standard deviation), particularly in the core region.

Finally, in practice, the vegetation branch does not occupy the entire outlet cross-section; its projected area spans approximately $y \in [-45, 45] \text{ mm}$. Within this region, the flow characteristics are relatively consistent across measurement planes, supporting the assumption that the sample is exposed to a stable and representative thermal environment.

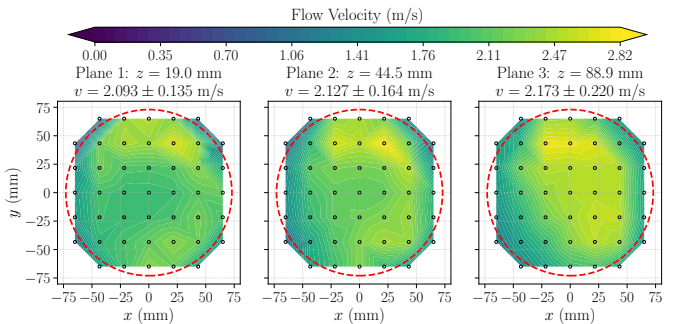


Figure A.20: Flow velocity contours measured at three vertical planes above the plenum outlet. Each panel shows the interpolated velocity field and average velocity within the core region, along with its experimental uncertainty.

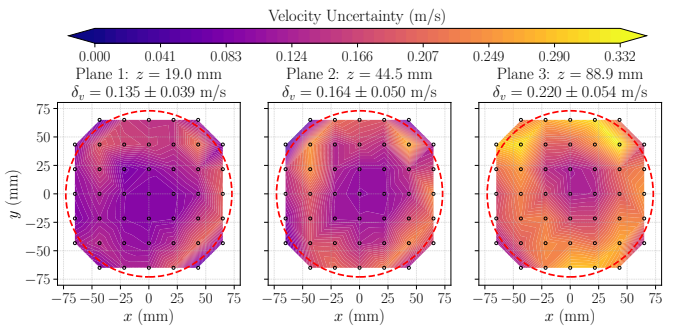


Figure A.21: Spatial distribution of velocity uncertainty at three heights above the plenum. Uncertainty combines statistical variation and propagated errors from pressure and temperature measurements.

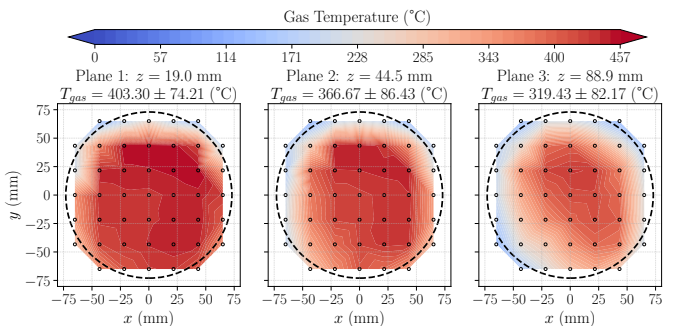


Figure A.22: Measured gas temperature contours at three vertical planes. A gradual decrease in temperature is observed with increasing distance from the plenum outlet, with moderate variability near the boundaries.

Appendix B. TGA kinetic analysis via KAS method

The kinetics of the degree conversion is given by

$$\frac{d\alpha}{dt} = A \exp\left(-\frac{E_a}{RT}\right) f(\alpha) \quad (\text{B.1})$$

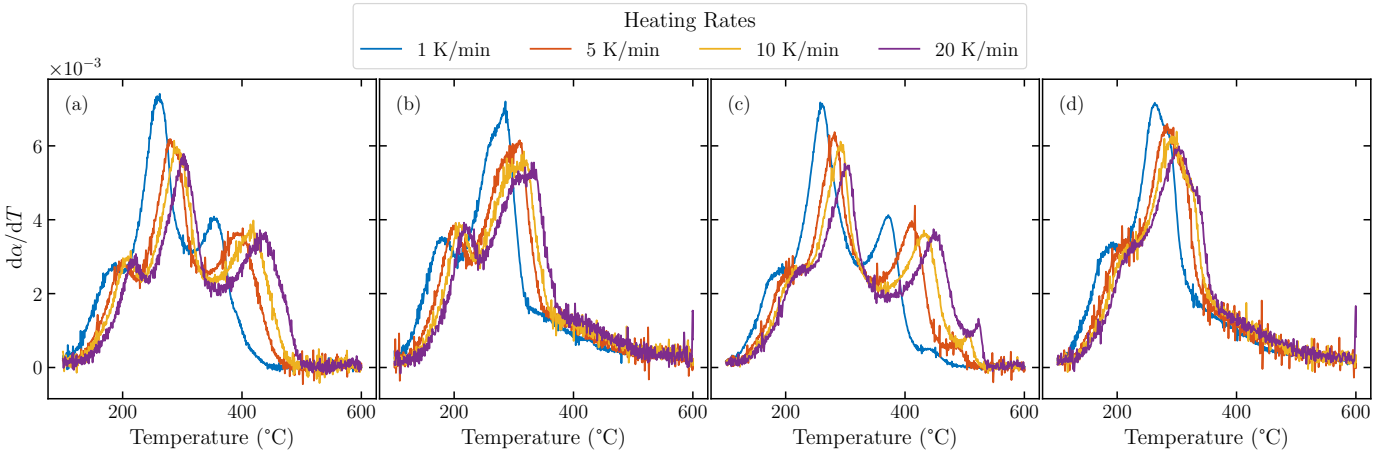


Figure B.23: DTG of bark and pine needles at different heating rates (a) pine needles in N_2 , (b) bark in N_2 , (c) pine needles in air, and (d) bark in air.

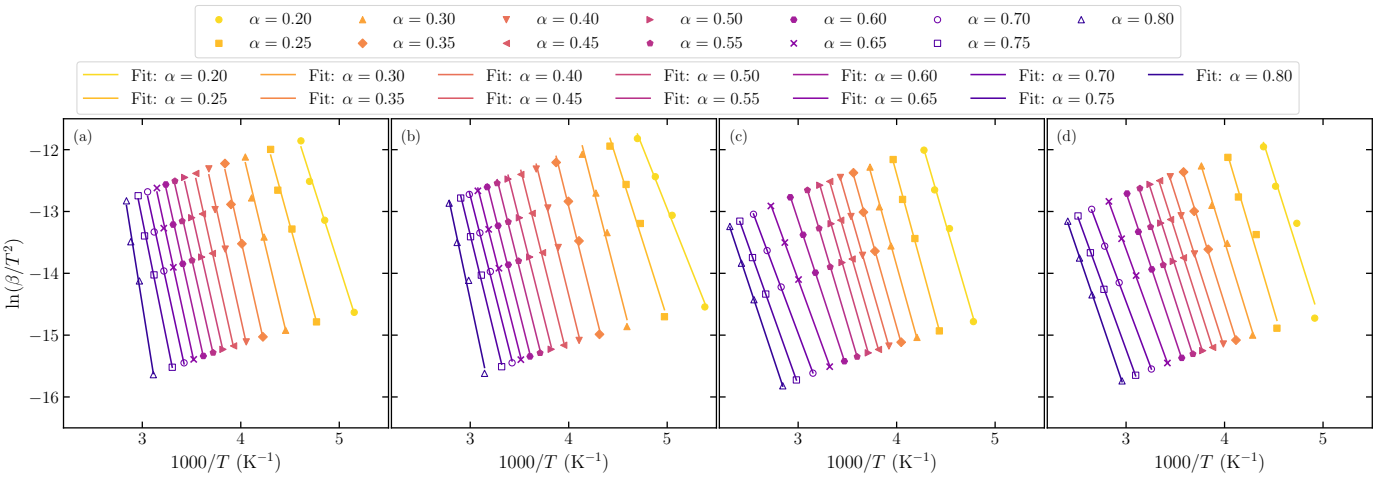


Figure B.24: KAS plot of TGA measurements of pine needles and bark. (a) pine needles in N_2 , (b) bark in N_2 , (c) pine needles in air, and (d) bark in air.

where $f(\alpha)$ is the differential reaction model, and R is the universal gas constant. The reaction model is chosen as the first-order reaction. Multiple reaction models can be chosen, however the first-order is chosen [55]. The differential form $f(\alpha)$ is $(1 - \alpha)^1$. When a constant heating rate β is implemented, the conversion degree change with temperature can be obtained as,

$$\frac{d\alpha}{dT} = \frac{A}{\beta} \exp\left(-\frac{E_a}{RT}\right) f(\alpha) \quad (B.2)$$

By integrating the equation, and assuming that the initial temperature and conversion degree to be zero, the integral form of reaction model defined as $g(\alpha) = -\ln(1 - \alpha)$, which can be expressed as

$$g(\alpha) = \int_0^\alpha \frac{d\alpha}{f(\alpha)} \cong \frac{A}{\beta} \int_0^T \exp\left(-\frac{E_a}{RT}\right) dT \quad (B.3)$$

The approximation in the equation implies first-order reaction approximation. The expression of the linear isoconversional developed by Kissinger-Akahira-Sunose (KAS) [55] with a given

conversion degree and a heating rate follows,

$$\ln\left(\frac{\beta}{T^2}\right) = \ln\left(\frac{AR}{E_a g(\alpha)}\right) - \frac{E_a}{RT} \quad (B.4)$$

By plotting $\ln(\beta/T^2)$ as a function of $-1/T$ for different heating rates, the activation energy can be obtained as the slopes for each given conversion degree. Moreover, the pre-exponential factor can also be obtained once the activation energy is known:

$$A = \frac{E_a \exp(b) g(\alpha)}{R} \quad (B.5)$$

Differential mass loss (DTG) thermograms of pine needles and bark at four heating rates under nitrogen (Figs. B.23a,b) show three regimes: water evaporation, active, and passive pyrolysis. Water evaporates below 100 °C. Hemicellulose and cellulose decompose in active and passive pyrolysis, while lignin decomposes in both, preventing a distinct peak [70]. Bark exhibits a more intense first peak and a higher-temperature second peak, reflecting compositional differences.

DTG data in air (Figs. B.23c,d) show an additional peak from char oxidation. Compared to nitrogen, pyrolysis peaks shift to lower temperatures due to oxidation-enhanced mass loss.

KAS plots (Fig. B.24) were used to derive activation energies from slopes and pre-exponential factors from intercepts. The method's reliability was confirmed by R^2 values of 0.97–0.99, indicating strong agreement with the linear model.

1605